

X-ray Resonant Scattering Studies of Orbital and Charge Ordering in

 $\text{Pr}_{1-x}\text{Ca}_x\text{MnO}_3$ M. v. Zimmermann¹, C. S. Nelson¹, J. P. Hill¹, D. G. Gibbs¹,M. Blumel¹, D. Casa², B. Keimer², Y. Murakami³, C.-C. Kao⁴,C. Venkataraman⁵, T. Gogoi⁵, Y. Tomioka⁶ and Y. Tokura^{6,7}¹ Department of Physics, Brookhaven National Laboratory Upton, NY 11973-5000² Department of Physics, Princeton University Princeton, NJ 08544 and Max-Planck-Institut für Festkörperforschung 70569 Stuttgart, Germany³ Photon Factory, Institute of Materials Structure Science High Energy Accelerator Research Organization Tsukuba 305-0801, Japan⁴ National Synchrotron Light Source, Brookhaven National Laboratory Upton, NY 11973-5000⁵ CM-CAT, Advanced Photon Source, Argonne National Laboratory Argonne, IL 60439⁶ Joint Research Center for Atom Technology (JRCAT) Tsukuba 305-0033, Japan⁷ Department of Applied Physics, University of Tokyo Tokyo 113-0033, Japan

We present the results of a systematic x-ray scattering study of the charge and orbital ordering in the manganite series $\text{Pr}_{1-x}\text{Ca}_x\text{MnO}_3$ with $x=0.25, 0.4$ and 0.5 . The temperature dependence of the scattering at the charge and orbital wavevectors, and of the lattice constants, was characterized throughout the ordered phase of each sample. It was found that the charge and orbital order wavevectors are commensurate with the lattice, in striking contrast to the results of earlier electron diffraction studies of samples with $x=0.5$. High momentum-transfer resolution studies of the $x=0.4$ and 0.5 samples further revealed that while long-range charge order is present, long-range orbital order is never established. Above the charge/orbital ordering tem-

perature T_0 , the charge order fluctuations are more highly correlated than the orbital fluctuations. This suggests that charge order drives orbital order in these samples. In addition, a longitudinal modulation of the lattice with the same periodicity as the charge and orbital ordering was discovered in the $x=0.4$ and 0.5 samples. For $x=0.25$, only long-range orbital order was observed with no indication of charge ordering, nor of an additional lattice modulation. We also report the results of a preliminary investigation of the loss of charge and orbital ordering in the $x=0.4$ sample by application of a magnetic field. Finally, the polarization and azimuthal dependence of the charge and orbital ordering in these compounds is characterized both in the resonant and nonresonant limits, and compared with the predictions of current theories. The results are qualitatively consistent with both cluster and LDA+U calculations of the electronic structure.

I. INTRODUCTION

Interest in the origins of high temperature superconductivity and colossal magnetoresistance in the transition metal oxides has driven much of the activity currently at the center of condensed matter physics. An important aspect of these strongly correlated electron systems is that no single degree of freedom dominates their response. Rather, the ground state properties are thought to reflect a balance among several correlated interactions, including orbital and charge ordering, magnetism, and coupling to the lattice.

The perovskite manganites provide an especially illuminating example of the interplay among these interactions, since in these materials the balance may be conveniently altered, for example by doping or through an applied magnetic field. As a result, much work has been done to understand their magnetic ground states and lattice distortions, dating back to the seminal experiments of Wollan and Koehler [1]. Less is known about the roles of charge and orbital order in these materials. The classic work of Goodenough [2] has nevertheless served as a guide to their ordered arrangements, as supplemented, for example, by detailed measurements of the crystal structure and of the temperature dependence of the lattice constants (see references [3,4], for example).

This situation has changed during the last two years following the detection of orbital and charge order by resonant x-ray scattering techniques [5,6,7,8,9,10,11]. Specifically, it has been found that the sensitivity of x-ray scattering to these structures can be significantly enhanced by tuning the incident x-ray energy to the transition metal K-absorption edge. Thus, it appears possible to characterize the orbital and charge ordering on a microscopic scale, and to study their response to changes of temperature or to an applied magnetic field. Insofar as we are aware, resonant x-ray scattering studies of these materials have now been extended to include $\text{La}_{0.5}\text{Sr}_{1.5}\text{MnO}_4$ [5], LaMnO_3 [6], $\text{La}_{1-x}\text{Sr}_x\text{MnO}_3$ [10,12], $\text{Pr}_{1-x}\text{Ca}_x\text{MnO}_3$ [13], V_2O_3 [14], YTiO_3 [15], LaTiO_3 [16], $\text{LaSr}_2\text{Mn}_2\text{O}_7$ [17], DyB_2C_2 [18,19], and $\text{Nd}_{0.5}\text{Sr}_{0.5}\text{MnO}_3$ [20,21], (and this list continues to grow). There is, in addition, an ongoing discussion of whether it is more appropriate to treat the resonant cross-section within an extended, band

structure description of the electronic structure, or instead with a more localized, atomic description [9,22,23,11]. A related question concerns how to write the resonant cross-section explicitly in terms of the order parameters for orbital and charge ordering.

In this paper, we present x-ray scattering studies of $\text{Pr}_{1-x}\text{Ca}_x\text{MnO}_3$ with $x=0.25, 0.4$ and 0.5 . Detailed studies have been made of the temperature dependence of the orbital and charge order scattering of all three samples, including characterization of the intensities, wavevectors, correlation lengths and lattice constants. Below a doping-dependent ordering temperature T_o , it is found that the charge and/or orbital order wavevectors are commensurate with the lattice at all temperatures. This contrasts with the results of electron diffraction studies of samples with $x=0.5$, where a significant variation of the charge order wavevector was reported near T_o [24,25]. Surprisingly, our high momentum-transfer resolution studies reveal that long-range orbital order is never established in the $x=0.4$ and 0.5 samples, although long-range charge order is observed in both. Further, for temperatures above T_o , the charge order fluctuations are longer ranged than the orbital fluctuations, suggesting that the charge ordering drives the orbital ordering in these systems. Recent Landau theories of the phase transition are consistent with this picture [26]. In contrast, for $x=0.25$ we observe long-range orbital order, with no indication of any charge ordering. We have also monitored the destruction of charge and orbital ordering after the application of a magnetic field in the $x=0.4$ sample. A similar phenomenology is found for increasing magnetic field as occurs for increasing temperature.

Finally, detailed measurements of the polarization and azimuthal dependence of the charge and orbital ordering have been carried out in both the resonant and nonresonant limits. In the π channel at the orbital wavevector of all three samples, we find that the resonant cross-section is qualitatively consistent with the results obtained earlier for LaMnO_3 [6] and with the predictions of both the localized and band-structure descriptions of the electronic structure. Likewise, we have found that the resonant scattering at the charge order wavevector is consistent with earlier results obtained for $\text{La}_{1.5}\text{Sr}_{0.5}\text{MnO}_4$ [5]. We have, in addition, discovered scattering in the π channel at the charge and orbital

wavevectors of the $x = 0.4$ and 0.5 samples. On the basis of its polarization and Q -dependence, we have deduced that it originates from a longitudinal lattice modulation. Earlier studies of $\text{La}_{0.5}\text{Ca}_{0.5}\text{MnO}_3$, had previously found a transverse modulation [4,27,28,29], and a similar modulation has been assumed in $\text{Pr}_{1-x}\text{Ca}_x\text{MnO}_3$. A summary of the present work was published earlier [13].

The organization of this paper is as follows. The experimental set-up is described immediately below, followed by a brief description of charge and orbital ordering in $\text{Pr}_{1-x}\text{Ca}_x\text{MnO}_3$. A simple model of the resonant orbital cross-section is given in Section IV. Our main results and discussion follow in Section V, which is divided into A. Diffraction Pattern, B. Resonant Scattering, C. Temperature Dependence, and D. Magnetic Field Dependence. A brief summary is given at the end.

II. EXPERIMENTAL

The single crystals used in the present experiments were grown by float zone techniques at JRCAT. $(0,1,0)$ surfaces were cut from cylinders of radius 3 mm, and polished with fine emery paper and diamond paste. The mosaic widths of the samples as characterized at the $(0,2,0)$ bulk Bragg reflections (in orthorhombic notation) were $0.1, 0.25$, and 0.25 , (FWHM), for the $x = 0.25, 0.4$ and 0.5 samples, respectively. These values varied by small amounts as the beam was moved across each sample surface, reflecting its mosaic distribution. The growth techniques and basic transport properties of these crystals have been described in detail elsewhere [30,31,32].

Most of the x-ray scattering experiments were carried out at the National Synchrotron Light Source on Beam lines X22C, X22B and X21. X22C is equipped with a bent, toroidal focussing mirror and a Ge(111) double crystal monochromator arranged in a vertical scattering geometry. This gives an incident linear polarization of 95% (ϵ) and an incident energy resolution of about 5 eV at the Mn K edge (6.545 keV). Three different detector configurations were used. Low momentum-transfer resolution scans employed slits before

the detector, and provided a longitudinal resolution of 0.0021 \AA^{-1} (FWHM) at the (010) reflections of each sample. High-resolution scans employed a standard Ge(111) crystal, and gave a longitudinal resolution of $4.5 \times 10^{-4} \text{ \AA}^{-1}$ (FWHM) at the respective (010) reflections. The third configuration provided linear polarization analysis of the scattered beam via rotation of a Cu(220) crystal about the scattered beam direction [33]. It gave longitudinal resolutions of 0.0069 \AA^{-1} and 0.0052 \AA^{-1} (FWHM) in the θ and ω geometries, respectively. For an incident photon energy set at the Mn K absorption edge, the Cu(220) scattering angle is 95.6° . This leads to a 5-10% uncertainty in the polarization-dependent intensities due to incomplete suppression of the unselected component of the scattered beam, and the small ω -component of the incident beam.

Magnetic field experiments were performed at NSLS X22B, which supports a bent, toroidal mirror and a single crystal Ge(111) analyzer-monochromator combination. As a result of mechanical restraints, the incident photon energy could not reach the Mn K edge. These experiments were, therefore, carried out in the nonresonant limit, with an incident photon energy of 8 keV. The sample was mounted in a 13 T superconducting magnet oriented in a horizontal scattering geometry. In addition, two series of experiments were performed on NSLS Wiggler beam line X21, which was equipped with a 4-bounce Si(220) monochromator and a focussing mirror, leading to extremely good incident energy resolution of 0.25 eV. One set of experiments was carried out on undulator beam line 9ID at the Advanced Photon Source. The optics for 9ID was comprised of a double crystal Si(111) monochromator and a π antiharmonic rejection mirror.

III. PROPOSED ORBITAL AND CHARGE ORDERED STRUCTURES

At room temperature, the crystal structure of $\text{Pr}_{1-x}\text{Ca}_x\text{MnO}_3$ is orthorhombic ($Pbnm$), as illustrated in Figure 1. Characteristic of the perovskite manganites, each Mn atom lies at the center of the octahedron defined by the oxygen atoms at the corners. Single layers of Pr atoms lie between the layers of octahedra. Depending on the temperature, there may

be distortions of the octahedra and tilts as is also illustrated in Fig. 1. The solid line in the figure outlines the orthorhombic unit cell.

A schematic phase diagram for $\text{Pr}_{1-x}\text{Ca}_x\text{MnO}_3$ versus Ca concentration and temperature [3,31] is shown in Figure 2. For small x ($0.15 \leq x \leq 0.3$) and at low temperatures, $\text{Pr}_{1-x}\text{Ca}_x\text{MnO}_3$ is a ferromagnetic insulator, and is believed to exhibit an orbitally ordered ground state analogous to that observed in LaMnO_3 . The electronic configuration of the Mn^{3+} (d^4) ions is (t_{2g}^3, e_g^1) with the t_{2g} electrons localized at the Mn sites. The e_g electrons are hybridized with the oxygen 2p orbitals, and believed to participate in a cooperative Jahn-Teller distortion of the MnO_6 octahedra. This leads to a $(3x^2 - r^2) - (3y^2 - r^2)$ -type of orbital order of the e_g electrons in the ab plane with the oxygens displaced along the direction of extension of the e_g orbitals. A schematic illustration of this orbitally ordered state for $x=0.25$ is shown in Figure 3a [3], with the orbital unit cell marked by the solid line. The excess Mn^{4+} ions in this material are believed to be disordered. It is noteworthy that the orbital period is twice that of the fundamental Mn spacing, so that orbital scattering appears at structurally forbidden reflections. In orthorhombic notation, for which the fundamental Bragg peaks occur at $(0, 2k, 0)$, the orbital scattering then occurs at $(0, k, 0)$.

Recently, the possibility of the existence of both charge and orbital ordering at $x=0.25$ has been suggested by various theoretical approaches [34,35]. Mizokawa, et al. [34] studied a related material, $\text{La}_{1-x}\text{Sr}_x\text{MnO}_3$, and found an ordered arrangement of $(3x^2 - r^2) - (3y^2 - r^2)$ and $(3z^2 - r^2)$ type orbitals surrounding the Mn^{4+} sites at $x=0.25$. While this structure is inconsistent with the magnetic structure in $\text{Pr}_{0.75}\text{Ca}_{0.25}\text{MnO}_3$, it first raised the possibility of structures other than those proposed by Jirak, et al. [3]. As discussed below, however, we have found no evidence for this type of charge ordering.

For Ca concentrations $0.3 \leq x \leq 0.7$, $\text{Pr}_{1-x}\text{Ca}_x\text{MnO}_3$ becomes an antiferromagnetic insulator at low temperatures (see Figure 2), and exhibits colossal magnetoresistance in applied magnetic fields, with the metal-insulator transition occurring between 5 and 8 T [31]. These effects result from charge ordering among the Mn^{3+} and Mn^{4+} ions, which occurs in addition to orbital ordering. The large conductivity is enabled through the hopping of e_g electrons

among Mn sites. The fraction of Mn ions in the Mn^{4+} state is determined largely by the concentration of Ca ions. Thus, by varying the Ca concentration, it is possible to alter the balance between charge and orbital ordering. The proposed ground state [3] for both the $x=0.4$ and $x=0.5$ concentrations is shown in Figure 3b. The small filled circles represent the Mn^{4+} ions, with one fewer electron than is localized at the Mn^{3+} sites. The solid line indicates the unit cell for orbital ordering, while the dashed line gives that for charge ordering. It is interesting that the proposed structures for $x=0.4$ and 0.5 are identical [3] and commensurate with the lattice, independent of concentration. Clearly, at least for $x=0.4$, this picture cannot be strictly correct. Jirak et al. proposed that the extra electrons present at $x=0.4$ could be accommodated in such a structure by a partial occupancy of the $3z^2 - r^2$ orbitals of the nominal Mn^{4+} sites. Other possibilities include small Mn^{3+} rich regions, higher order structures, or small regions of orbital disorder. As discussed below, our data reveal that, in fact, the orbital order is not long-ranged in either of these compounds, although the charge order is. In the orthorhombic notation, the charge order reflections occur at $(0, 2k+1, 0)$ and the orbital order reflections at $(0, k+1/2, 0)$. Note that the orbital period ($= 2b$) in the $x=0.4, 0.5$ compounds differs from that occurring in samples with $x < 0.3$ ($= b$), as a result of the presence of charge ordering.

The magnetic structure of these compounds at low doping ($0.15 \leq x \leq 0.3$) is ferromagnetic with $T_C \approx 140$ K. Compounds with higher doping ($0.3 \leq x \leq 0.75$) are CE-type antiferromagnets with $T_N = 170$ K for x between 0.4 and 0.5 [3]. The in-plane components of the magnetic structures are also illustrated in Figure 3.

IV. RESONANT CROSS-SECTION FOR ORBITAL ORDERING {A SIMPLE MODEL

The present experiments were carried out using x-ray resonant scattering techniques. As shown in a series of recent papers [5,6,7,8,9,10,22,12,20,23,11], the sensitivity of x-ray scattering to orbital ordering in the transition metal oxides is enhanced when the incident x-

ray energy is tuned near the K-absorption edge. In the resonant process, a core level electron is promoted to an intermediate excited state, which subsequently decays. This can lead to new scattering mechanisms, such as resonant magnetic scattering. In that case, the excited electron is promoted to a partially occupied orbital and the sensitivity to the magnetic polarization arises through the exchange interaction [36,37]. In the present case, we consider a dipole process involving a Mn 1s to 4p transition. In the simplest model, it is assumed that the 4p_{x,y,z} states are initially unoccupied, but split in the orbitally ordered state (see figure 4). This gives rise to a nonzero resonant scattered intensity at reflections sensitive to the difference between the two orbitally ordered sublattices. This model, summarized below, is designed to capture the essence of the problem, but not the details of the interactions for which a more sophisticated theory is required. For example, recent LSDA + U calculations [9] suggest that the 4p bands are not split per se, but rather experience changes in the weight of the density of states in the ordered phase. Nevertheless, our model is conceptually simple, and reproduces most of the systematics of the data.

For a difference reflection, the resonant scattered intensity may be written [6]:

$$I^{\text{res}} = \sum_{x,y,z,n=-1}^X \frac{\langle s | \hat{P}_n | p_m \rangle \langle p_m | \hat{P}_n | j \rangle}{\Gamma_0 \Gamma_m + i = 2} e^{i\phi} ; \quad (1)$$

where the coordinate system has been chosen so that x and y are along the direction of extension of the ordered e_g orbitals and z is perpendicular to the x-y plane (see Figure 4). $|j\rangle$ and $|p\rangle$ are the wavefunctions of the Mn 1s and 4p orbitals, respectively. \hat{P} is the component of the dipole operator ($\hat{P} = x, y, z$). Γ_0 is the incident photon energy and Γ_m is the energy of the unperturbed p_m levels. The incident (final) polarization of the photons is (ϵ_i) and $n = -1$ labels the orbital sublattice. Γ_m is the lifetime of the excited state. Note, $\langle p_m | \hat{P}_n | j \rangle = A_m$, where A is a constant. As illustrated in the figure, $\Gamma_m = \Gamma_0$ for $n = +1, m = x, z$; $\Gamma_m = 2\Gamma_0$ for $n = +1, m = y$; and so on.

The origin of the splitting is not specified in our model. Two mechanisms (both consistent with the measurements) have been discussed, and indeed, the discussion has sparked some controversy [5,6,7,8,9,10,22,12,21,23,11]. One possible origin involves the Coulomb

coupling of the Mn 3d and 4p levels, either directly or indirectly through the hybridization of the Mn (3d)-O (2p) and O (2p)-Mn (4p) states [23]. The latter effect has the same sign as the direct Coulomb interaction, but is expected to be smaller [23]. In this picture, the Coulomb coupling raises the $4p_m$ levels lying parallel to the direction of extension of the orbital (by 2 in our model) and lowers those lying perpendicular (by 1) as shown in Figure 4. Detailed calculations using atomic orbitals by Ishihara and Maekawa [23] have found qualitative consistency with all of the known experimental results for $\text{La}_{1-x}\text{Sr}_x\text{MnO}_4$ [5], LaMnO_3 [6], $\text{Pr}_{1-x}\text{Ca}_x\text{MnO}_3$ [13], and $\text{La}_{1-x}\text{Sr}_x\text{MnO}_3$ [10]. Alternatively, the motion of the oxygen atoms away from regions of high charge density through the Jahn-Teller interaction lowers the energy of the $4p_m$ levels lying parallel to the direction of the extension of the orbital, and raises those lying perpendicular. This effect thus has the opposite sign to that of the 3d-4p Coulomb interaction discussed above, and in fact these mechanisms compete with each other. Several groups have argued that the oxygen motion is the dominant effect leading to resonant scattering at the orbital wavevector [9,22,11,38,39]. Calculations of the resonant cross-section based on such approaches, and utilizing band structure descriptions of the 4p density of states in LaMnO_3 (which show changes in weight, rather than a simple splitting) also reproduce the main experimental facts and further, make detailed predictions about the resonant line structure measured in x-ray scattering experiments [9,13]. Insofar as we are aware, the experimental data obtained to date do not distinguish either theoretical approach conclusively, and this remains an open question. For the purpose of calculating the resonant cross-section of our simplified model, however, all that is required is that $\epsilon \neq 0$.

We stress that regardless of which of the two microscopic mechanisms is the dominant one, the resonant scattering will reflect the symmetry of the orbital ordering through the perturbation of the local electronic states at the Mn^{3+} sites. We believe this is true even though the d orbitals are not directly involved as intermediate states in the resonant process. In particular, in terms of the Jahn-Teller distortion considered above, the orientation of the e_g orbitals and the oxygen motion reflect the same order parameter. It follows that the peak positions and widths determined in the x-ray experiments measure the orbital

periodicity and correlation lengths, respectively. However, it still remains to interpret the x-ray peak intensities on an absolute scale, which will require additional calculations. From this perspective, we think of the resonant scattering as Templeton scattering arising from the anisotropic charge distribution induced by orbital ordering. Its basic properties, for example the polarization and azimuthal dependence, are then determined by the anisotropy of the susceptibility tensor (which in the dipole approximation is a second rank tensor).

Working in a linear polarization basis, with polarization perpendicular to the scattering plane and parallel, it is easy to show that for a θ incident beam, the resonant cross-section for an orbital reflection of the type considered here, does not give rise to a θ polarized scattered beam. That is, for any azimuthal angle ϕ , $I_{\theta}^{\text{res}} = 0$. In the rotated θ channel, it may be further shown that:

$$I_{\theta}^{\text{res}}(\phi) = \frac{A^4 \sin^2 \theta}{[\sin^2 \theta + 4(2 - \cos^2 \theta)^2][\sin^2 \theta + 4(\cos^2 \theta + \cos^2 \theta)^2]} \quad (2)$$

where $\cos \theta = (\mathbf{k} \cdot \mathbf{c})/k$. This simple model thus predicts that the scattering is all of the θ type and that it has a twofold azimuthal symmetry, with zeros coming when the incident polarization is parallel to the c-axis. The azimuthal angle characterizes rotations of the sample about the scattering wavevector, and is defined to be zero when the c-axis is perpendicular to the scattering plane (figure 4). Although a detailed analysis of the data requires a more sophisticated treatment, this model captures many of the essential elements of the experimental results, as will be shown below.

It's worth adding that there should also be nonresonant scattering from an orbitally ordered material. However, for the structures shown in Figure 3, and the $(0,k,0)$ reflections, the charge density is arranged symmetrically, and the scattering is zero. It is nevertheless still possible that nonresonant charge scattering can arise at the orbital wavevector from lattice modulations accompanying the orbital ordering, and such a modulation has been observed in $\text{Pr}_{1-x}\text{Ca}_x\text{MnO}_3$ (see e.g., [3,40,41]) and in $\text{La}_{0.5}\text{Ca}_{0.5}\text{MnO}_3$ [4,27,28,29]. In fact, one result of the present work is the observation of a longitudinal component of this modulation for the $x=0.4$ and 0.5 samples, which we will also discuss below.

V . R E S U L T S

A . D i r a c t i o n P a t t e r n

Scans of the resonant scattering intensity versus momentum transfer along the $(0,k,0)$ direction are shown for the $x=0.25$ and $x=0.4$ samples, respectively, in Figures 5a and 5b. Results for the $x=0.5$ sample are similar to those shown for $x=0.4$, and are not shown. In each case, the samples were cooled below their ordering temperatures, to $T=300$ K and $T=30$ K for the $x=0.25$ and the $x=0.4$ samples, respectively. The intensities are plotted versus k in counts per second and shown on a logarithmic scale. Twinning within the ab -plane was observed in all three samples. It is visible as a peak splitting in low momentum-transfer resolution scans, such as shown in Figure 5a for the $x=0.25$ sample. This splitting is not observed in high-resolution scans, for which the resolution volume never overlaps the second peak (see Figure 5b).

The large peaks falling at $k=2,4$ in both scans in Figure 5 correspond to bulk allowed Bragg reflections expressed in orthorhombic units. Their intensities were obtained using Al absorbers, and should be considered qualitative. Referring to the $x=0.25$ sample (Figure 5a), the peaks at $k=1,3$ correspond to orbital ordering with the periodicity defined in Figure 3a. Count rates of 400/sec were obtained at the $(0,1,0)$ reflection on the NSLS X21 Wiggler beam line. For the $x=0.4$ sample, the peaks at $k=0.5, 1.5$ and 2.5 correspond to orbital ordering, while those at $k=1,3$ correspond to charge ordering, both with the periodicities defined in Figure 3b. Typical count rates for this sample obtained at the NSLS bending magnet beam line X22C reached 1500/sec at the (010) reflection and 3000/sec at the $(0,1.5,0)$ reflection. Considering the many differences between the two beam lines and the geometries employed, we have not attempted to make quantitative comparisons of the intensities. The origins of the peaks at $k=0.65$ and 1.4 are unknown. Both peaks persisted in the diffraction pattern above the charge and orbital ordering temperatures, however, and were not studied further.

It's clear from the figure that the wavevectors for charge and orbital ordering in all three samples are simply commensurate with the lattice, and independent of concentration. Further, the measured peak positions are all consistent with the periodicities proposed in Figure 3 for the different orbital and charge ordered structures. The temperature dependence of the charge and orbital order wavevectors will be discussed further in Section V c. below.

B. Resonant Scattering

1. Orbital Wavevector

Figure 6 shows the energy dependence of the scattering at the (100) orbital wavevector of the $x=0.25$ sample as the incident x-ray energy is tuned through the Mn K absorption edge (6.539 keV). These data were obtained with a Si(111) analyzer on the CM C-CAT undulator beam line 9ID at the APS. A large resonant signal is visible at $h\nu = 6.547$ keV, reaching more than 20,000 counts per second near the edge. In addition, there are two smaller peaks at higher energies ($h\nu = 6.56$ and 6.575 keV), and one below (at $h\nu = 6.534$ keV). The inset shows the lower energy peak in more detail. No signal was observed at energies 100 eV above or below the absorption edge, implying that only pure resonant scattering was present in this sample. Polarization analysis (performed on bending magnet beam line X22C at the NSLS) suggests that the scattered signal is predominantly polarized, consistent with a rotation of the incident linear polarization from being perpendicular to the diffraction plane, \perp , to lying within the diffraction plane, \parallel . It should be added that all of the data shown here, and in Figures 7, 10 and 11 below, were obtained at an azimuthal angle $\phi = 90^\circ$. As a function of azimuthal angle, the resonant intensity observed for the $x=0.25$ sample takes maxima at $\phi = 90^\circ$ and 270° , and minima at 0° and 180° . These results are all similar to those obtained previously at the orbital wavevector of LaMnO_3 , including the 4-peaked line structure in the energy dependence, an identical polarization and azimuthal dependence, and the absence of nonresonant scattering away from the edge [5,42].

Figures 7a and 7b show the energy dependence of the scattering at the (0,1.5,0) and (0,2.5,0) orbital wavevectors of the $x=0.4$ sample, again as the incident x-ray energy is tuned through the Mn K absorption edge. These data were obtained on the X22C bending magnet beam line at the NSLS, and explicitly resolve the polarization. The closed circles show the σ scattering, and the open circles show the π scattering. Although the structure in figure 7a is not as clearly resolved as in the $x=0.25$ sample, the main features of the π scattering are similar, including a pronounced resonance peak at 6.547 keV and a weaker peak at 6.57 keV. In contrast to the σ scattering, the π

scattering shows a double peaked structure with a pronounced dip at the absorption edge. This is strongly reminiscent of the behavior of charge scattering, and suggests the presence of a lattice modulation with the orbital wavevector. The fact that the π intensity does not fall off at lower x-ray energy, but instead continues above background, is further evidence of a significant nonresonant signal as would be produced by such a modulation. Lattice modulations associated with the CE type structure have been observed before in $\text{Pr}_{1-x}\text{Ca}_x\text{MnO}_3$ e.g. [3,25,40,41] and also in $\text{La}_{0.5}\text{Ca}_{0.5}\text{MnO}_3$ [4,19,21]. In the latter compound, the structure was solved, and the modulation found to be purely transverse. Such a modulation, however, is inconsistent with the present results. We will return to this point below.

A broader ranged energy scan of the (0,2.5,0) orbital wavevector is shown for the $x=0.4$ sample in Figure 8. These data were taken with a Ge(111) analyzer, and are plotted versus energy for several different azimuthal angles. The use of a Ge analyzer implies that both σ and π components are detected, and that their intensities add. Referring to the scan for $\phi = 85^\circ$, the basic features shown in Figure 7b are reproduced, although the π scattering clearly dominates the signal. Below the Mn absorption edge, the observed scattering is approximately constant until it reaches the Pr L_2 absorption edge energy at 6.43 keV. There the intensity again shows a dip, primarily as a result of the increase in the absorption. Qualitatively similar results were obtained for the $x=0.5$ sample.

It's clear from Figure 8 that except for a variation of the overall intensity, no new features

are introduced as a function of azimuthal angle. A quantitative study of the azimuthal dependence of the orbital scattering at $(0, 2.5, 0)$ is shown in Figure 9, in which the maximum resonant intensity in the π geometry was recorded versus azimuthal angle for rotations over 180° . The data have been normalized by the average intensity of the $(0, 2, 0)$ and $(0, 4, 0)$ fundamental Bragg reflections to correct for small variations due to sample shape. Again, $\phi = 0$ corresponds to a configuration in which the c -axis is perpendicular to the diffraction plane. In contrast to a normal charge reflection, for which the intensity is independent of the azimuthal angle, the resonant scattering exhibits a characteristic oscillation with a two-fold symmetry. The intensity approaches zero when $\phi = 0$ and 180° , consistent with the π polarized component of the resonant scattering in the $x = 0.25$ sample. The solid line in Figure 8 is a fit to the form $A \sin^2 \phi$, as predicted in equation 2.

To summarize: In all three samples, we find a pure resonant signal in the π channel at the appropriate orbital wavevector with the dominant peak located near the Mn K absorption edge. Additional π structure is observed both above and below the absorption edge. The π -resonant scattering has the characteristic azimuthal dependence, varying as $\sin^2 \phi$, where ϕ is the azimuthal angle. These results are identical to what has been observed previously in LaMnO_3 [6] and $\text{La}_{0.5}\text{Sr}_{1.5}\text{MnO}_4$ [5]. In the $x = 0.4$ and 0.5 samples, there is in addition a π component of the scattering at the orbital wavevector with both resonant and nonresonant parts. The non-resonant component lacks any azimuthal dependence and is consistent with normal charge (or Thomson) scattering. The $x = 0.25$ sample lacks a π component to within the detection limits of the experiment, as was also the case in LaMnO_3 .

We associate the dominant, resonant peak, which occurs in the π channel of all three samples with the electric dipole transition coupling $1s$ and $4p$ states, as discussed in section IV. Recall that the sensitivity to orbital ordering may be thought of, qualitatively, as arising from a splitting of the Mn $3d$ states, either through the Jahn-Teller distortion of the oxygen atoms or through a Coulomb interaction. In either case, the existence of a dipole resonance in the π channel, and the observed azimuthal dependence, are consis-

tent with theoretical predictions. We, therefore, interpret the observed resonant scattering as Templeton scattering induced by the orbital ordering, just as previously concluded for LaMnO_3 and $\text{La}_{0.5}\text{Sr}_{1.5}\text{MnO}_4$ [5,6]. To explain the additional fine structure both above and below the main peak, however, requires a more sophisticated treatment. ElMOV et al. [9], in particular, have performed band structure calculations for LaMnO_3 with a LSDA+U-type approach, and shown that the fine structure above the absorption edge reflects the 4p density of states after hybridization of the central Mn 4p and surrounding O 2p states. They show further that the higher energy peaks originate predominantly from the Jahn-Teller distortion of the oxygens, and not from direct Coulomb interactions. In contrast, the small peak about 13 eV below the white line is associated with the intersite 4p-3d hybridization of the central and neighboring Mn ions via the intervening O 2p states. Although quantitative comparisons remain to be made, the qualitative agreement between these predictions and the observed spectra is good, and offers a natural description of the experimental results. In this regard, it should be added that Ishihara et al. [43] have also carried out cluster calculations of the resonant cross-section in $\text{LaSr}_2\text{Mn}_2\text{O}_7$, assuming an intra-site 3d-4p Coulomb origin of the 4p splitting. By including band effects, they also were able to produce qualitatively similar fine structure above the Mn K edge. Thus, we are not able to distinguish a possible Coulomb origin of the resonant peak from a Jahn-Teller origin on the basis of our experiments | however, the additional fine structure at higher photon energies appears to result from band effects in both approaches.

It's worth noting that the energy of the pre-edge feature (see inset, fig. 6) corresponds to that of the Mn 3d states. Several groups have shown that this feature is highly sensitive to the 3d orbital occupancy [9,22,8,44], but not to the Jahn-Teller distortion (oxygen motion)—in contrast with the main-edge feature. In fact, states of both d- and p-like symmetry (with respect to the central ion) exist at the pre-edge energy, with significantly more weight in the d-like states [44], suggesting that both dipole and quadrupole processes should contribute. Takahashi, et al. estimate that the total intensity, enhanced by interference with the main-edge processes, is about 1% of the main edge. In our experiment, we find that the pre-edge

intensity is about 5% of the main edge intensity. In addition, we observed only a single feature, in contrast with the two features, separated by 3 eV, predicted by Takahashi, et al. [44]. Our energy resolution for these data was 1.5 eV. In principle, the pre-edge feature could exhibit different azimuthal [44] and temperature dependences from those of the main-edge feature. In our studies of the azimuthal and temperature dependence however, we found no difference between the pre-edge and main-edge behaviors, to within errors.

We note, in passing, that in V_2O_3 the resonant ion is not in a center of inversion symmetry and that, therefore, dipole transitions are allowed directly into the d-band of that material. This gives rise to a large pre-edge feature which has also been used to study orbital order [8,14] by x-ray scattering techniques.

We now turn to the lattice modulation observed at the orbital wave-vector in the Γ channel. Such modulations have been observed before in CE-type structures, and in particular in $Pr_{1-x}Ca_xMnO_3$ by neutron [3,25,41] and non-resonant x-ray scattering [41,45]. Similar results have also been obtained in $La_{0.5}Ca_{0.5}MnO_3$ [4] at $(h; \frac{k}{2}; 2n)$, where $h \neq 0$ and $k \neq 0$, the incommensurability, is weak (we have converted to Pbnm settings to be consistent with the rest of the present paper). The latter structure was solved by x-ray powder diffraction and a purely transverse modulation of the Mn^{4+} sites was deduced, wherein the Mn^{4+} sites are displaced along the a-direction with a periodicity equal to the orbital periodicity. All of the orbital superlattice peaks observed to date in the $Pr_{1-x}Ca_xMnO_3$ system have also had a significant a-axis component and a similar distortion has been assumed [3,25].

In the present case, the Γ scattering observed at $(0; k + \frac{1}{2}; 0)$ requires a longitudinal b-axis component of the modulation. This follows from the small-displacement limit of the x-ray intensity, which varies as Q to leading order for displacements of the form $\sin(\mathbf{R})$. For $x=0.4$ and 0.5 , we did not examine reflections of the form $(h/2, 0, l)$ with $l \neq 0$ and cannot draw conclusions about displacements in other directions, however, we have recently performed limited studies on an $x=0.3$ sample in which the orbital reflections around $(0, 2, 0)$ and $(2, 2, 0)$ were studied. The non-resonant scattering was observed to be significantly stronger in the vicinity of the (220) consistent with a larger transverse displacement and a

small longitudinal modulation [46]. We will return again to the lattice modulation shortly.

It is also worth commenting on the differences between the $\text{La}_{0.5}\text{Ca}_{0.5}\text{MnO}_3$ structure and the present case. In $\text{La}_{0.5}\text{Ca}_{0.5}\text{MnO}_3$, a temperature dependent incommensurability was observed at the orbital wavevector [9,24], whereas in the present case the scattering is strictly commensurate. The source of the incommensurability in the former material is believed to be an ordered array of domain walls – discommensurations – separating regions of commensurate order. As is discussed below, we observe domain walls at a similar spacing in $\text{Pr}_{0.5}\text{Ca}_{0.5}\text{MnO}_3$. Thus, the main difference between the two structures appears to be that the domain walls are ordered in $\text{La}_{0.5}\text{Ca}_{0.5}\text{MnO}_3$, but disordered in $\text{Pr}_{1-x}\text{Ca}_x\text{MnO}_3$. It is an interesting question as to why this is so.

2. Charge Order Wavevector

Figures 10a and 10b show the energy dependence of the scattering at the (0,1,0) and (0,3,0) charge order wavevectors of the $x=0.4$ sample, as the incident x-ray energy is tuned through the Mn K absorption edge. These data were obtained at the NSLS beam line X22C and are polarization resolved. The open circles show the σ scattering and the closed circles the π scattering. No signal was obtained in the π channel, to within the detection limits of the experiment. In the σ channel the (0,1,0) reflection has a shoulder at lower energy which rises to a resonant peak at 6.544 keV. This is followed by a dip and another smaller peak centered near 6.58 keV. The profile of the (0,3,0) reflection shows a resonant peak at slightly higher energy (6.546 keV) relative to the (0,1,0) reflection, and the additional structure appears inverted. This is a clear signature of an interference process, involving the resonant and nonresonant contributions to the charge order scattering. The nonresonant scattering may, in principle, result from the valence modulation itself (which is weak), or from an accompanying lattice modulation, or both. The resonant scattering arises from the anomalous parts of the Mn^{3+} and Mn^{4+} scattering factors, which are distinct.

For comparison, the energy dependence of the scattering at the charge order wavevector

(010) of the $x=0.5$ sample is shown in Figure 11. The data were obtained without an analyzer, and so include both the σ component and any π component. The lineshape is nearly identical to that obtained for the $x=0.4$ sample at the same reflections.

A series of broader ranged energy scans of the (0,3,0) reflection taken at various azimuthal angles for the $x=0.4$ sample is shown in Figure 8. The basic features noted in Figure 10 are reproduced there. In addition, there is a dip in the scattering at 6.44 keV, which reflects the Pr L_2 absorption edge. We believe that the peak at 6.64 keV in the scan at $\phi=0$ arises from multiple scattering and can be ignored. Except for a decrease of the resonant intensities, very little else changes in these spectra as a function of azimuthal angle, similar to what was observed for orbital ordering.

A quantitative study of the dependence of the charge order scattering on azimuth at the (0,3,0) reflection is shown in Figure 9. The filled squares record the behavior of the maximum resonant intensity obtained at 6.546 keV, while the open squares give the intensity of resonance at 6.47 keV. As before, these data have been normalized by the average of the (020) and (040) fundamental Bragg intensities. In contrast to the nonresonant charge order scattering, which is flat as expected, the resonant charge order scattering exhibits a pronounced azimuthal dependence, with the same sin-squared behavior as observed above for the resonant orbital scattering.

The explanation of this azimuthal dependence follows simply from the structure factor of (0,k,0) charge-type peaks:

$$f(0;2n+1;0) = f_{3A}^{n=1} + f_{3B}^{n=-1} - 2f_{4+}; \quad (3)$$

where $f_{3A(B)}^{n=1(n=-1)}$ are the atomic form factors for the Mn^{3+} ions on the A (B) orbital sublattice, and $n=1,-1$ refers to Figure 4. As emphasized above, these quantities are second rank tensors near resonance. We take f_{4+} to be spherically symmetric and we write

$$f_{3A} = \begin{matrix} & 0 & & 1 \\ \begin{matrix} B \\ \vdots \\ C \\ \vdots \\ A \end{matrix} & \begin{pmatrix} a & 0 & 0 \\ 0 & b & 0 \\ 0 & 0 & b \end{pmatrix} & \end{matrix}; \text{ and } f_{3B} = \begin{matrix} & 0 & & 1 \\ \begin{matrix} B \\ \vdots \\ C \\ \vdots \\ A \end{matrix} & \begin{pmatrix} b & 0 & 0 \\ 0 & a & 0 \\ 0 & 0 & b \end{pmatrix} : \quad (4)$$

where f_{3A} and f_{3B} have the symmetries $3x^2 - r^2$ and $3y^2 - r^2$, respectively. Calculating the polarization and azimuthal dependence of the scattering,

$$I = \sum_i |\tilde{F}_{0k0}(\theta)|^2 f_i^2; \quad (5)$$

we find a two fold azimuthal dependence in the $\theta = 0$ channel, with zeroes at $\phi = 0$ and 180° , as observed. In addition, equation 5 predicts a $\theta = 90^\circ$ component with a four-fold symmetry (with zeros at $0, 90, 180, 270^\circ$) although with a significantly smaller intensity (which we were unable to observe). We remark that it is the anisotropy of the structure factor $f(0, 2n+1, 0)$ that gives rise to the observed azimuthal dependence. In this sense, the "\charge-order" reflection has some orbital character.

In order to model the energy dependence of the charge order scattering, we write the structure factor as a sum of the scattering factors of the Mn^{3+} and Mn^{4+} ions within the unit cell, including both resonant and nonresonant terms for each. Here, for simplicity, we neglect the tensor character discussed above, and treat the form factors as (complex) scalars. Figure 12a shows schematic forms of the real and imaginary parts of the Mn^{3+} scattering factor, plotted versus incident photon energy. As our intention in the following was to gain a qualitative understanding of the energy lineshape, the parameters have been chosen for convenience of illustration, and do not represent the actual properties of Mn . The Mn^{4+} scattering factor is then obtained from that of Mn^{3+} by shifting the absorption curve by 2eV, following Murakami, et al. [5]. Assuming that the Mn displacements are along the b -axis with modulation wavevector $(0, k, 0)$ in the $x=0.4$ and 0.5 samples (see inset Figure 12b), the structure factor may be written:

$$f(0; k = \text{odd}; 0) = f_{3+} e^{ik} - f_{4+} e^{-ik}; \quad (6)$$

where δ is a displacement parameter (in units of b , the lattice constant). This reduces to the simple form $(f_{3+} - f_{4+})$ when $\delta = 0$, as expected.

A plot of the energy dependence of the intensity predicted by this model for the $(0, 1, 0)$ and $(0, 3, 0)$ reflections is shown in Figure 12b for $\delta = 0$ and including nonresonant scattering

arising from oxygen motion. It reproduces the basic features of the lineshapes in Figure 10, including the interference. The lineshapes also resemble those generated by Murakami et al. [5] for $\text{La}_{0.5}\text{Sr}_{1.5}\text{MnO}_4$, using a more quantitative model. If the manganese atoms are then allowed to move ($\neq 0$), the small shift of the peak maximum of the (0,1,0) reflection relative to the (0,3,0) reflection is also described. This is illustrated in Figure 12c. It is worth noting that a simple transverse displacement cannot explain the x-ray results for the charge ordering, just as was noted earlier for the modulation accompanying the orbital ordering. On the basis of these results, we conclude that the $x=0.4$ and 0.5 samples exhibit lattice modulations with displacements along the b -direction, and produce scattering at both the charge and orbital wavevectors. A fuller understanding of the lattice distortions observed in these materials will require further experiments.

C . Temperature Dependence

1. Intensities

The temperature dependence of the orbital ordering intensity between 10 and 850 K is shown for the $x=0.25$ sample in Fig. 13. Each point represents the peak intensity obtained from a k -scan of the (0,1,0) reflection, such as is shown in Fig. 5a. Circles and squares represent the results of two different runs, one taken at high temperatures with the sample heated in an oven and the other at low temperatures with the sample cooled in a cryostat. The two data sets were then scaled to be equal at 300 K. Referring to Fig. 13, the orbital intensity is approximately constant (to within 3 %) between 10 and 200 K, and decreases gradually with a long tail until about 850 K – a surprising result. High momentum-transfer resolution scans showed further that the orbital peak widths were independent of temperature and resolution-limited throughout the ordered phase. Thus, the intensities shown in Fig. 13 may be regarded as integrated intensities. The resolution-limited behavior also implies that the corresponding orbital correlation lengths were at least 2000 Å along

the b-direction.

The temperature dependences of the integrated charge and orbital ordering intensities of the $x=0.4$ sample are plotted between 10 and 300 K in Fig. 14a,b. The charge order intensities were obtained at the $(0,3,0)$ reflection both at resonance using a Ge(111) analyzer and off-resonance at 6.6 keV. The latter employed a Cu(220) analyzer. The orbital intensities were obtained at resonance at the $(0,1.5,0)$ reflection, where the resonant π scattering dominates the signal and off-resonance at the $(0,2.5,0)$ reflection, with an incident photon energy of 6.47 keV. Both data sets for the orbital ordering were obtained using a Ge(111) analyzer.

Referring to the figure, the orbital and charge intensities are approximately constant between 10 and 130 K, but begin to decrease above 130 K. They drop abruptly to zero at 245 K, consistent with a first order, or nearly-first-order, transition. It is clear from the figure that the temperature dependences of the resonant and nonresonant intensities are identical for the charge and orbital ordering, respectively, at least to within the present counting statistics. This suggests that the lattice modulation accompanying the charge and orbital ordering reflects the same order parameter. The temperature dependences of the charge and orbital ordering in the $x=0.4$ sample are also very similar, as shown directly in an earlier publication [13]. There we speculated that the charge and orbital ordering might be linearly coupled. More recently, Zhang and Wang have argued on the basis of a Landau theory that the charge and orbital ordering in $\text{Pr}_{1-x}\text{Ca}_x\text{MnO}_3$ are quadratically coupled [26], but that the coupling is sufficiently strong that they have very similar temperature dependences over the range considered here.

The temperature dependences of the orbital and charge order intensities of the $x=0.5$ sample between 10 and 300 K are shown in Fig. 15a,b. The orbital ordering intensities were again obtained from k -scans of the $(0,1.5,0)$ reflection using Ge(111) and Cu(220) analyzer configurations, with the latter in a π geometry. The signal rates in these experiments were weak, ($< 10/\text{sec}$ at $T=220\text{K}$), making a definitive characterization of the temperature dependence difficult. Charge order intensities were obtained at the $(0,1,0)$ reflection using

a Ge(111) analyzer. All of these data were obtained at the Mn K-edge resonance.

Referring to figures 15a and 15b, the orbital ordering intensity is approximately constant between 10 and 150 K, and begins to fall off between 150 and 200 K, reaching zero at about 250 K. The charge order intensity is also constant between 10 and 150 K, but exhibits a much clearer decrease near the Neel temperature $T_N = 170$ K. A similar decrease at T_N was observed for the orbital intensity of LaMnO_3 [6], where a correlation was made between the long-range antiferromagnetic order and the orbital order. Although this trend is suggested in each of the samples studied here, with $T_N = 140, 170$ and 180 in the $x = 0.25, 0.4$ and 0.5 samples, respectively, only the data for the charge ordering of the $x = 0.5$ sample is convincing. Despite repeated attempts to quantify this behavior in the other samples, we still cannot claim to have measured a definitive link between the magnetic ordering and the charge and orbital ordering in each case.

2. Correlation Length

High momentum transfer resolution longitudinal scans of the Bragg, charge and orbital ordering lineshapes of the $x = 0.4$ and 0.5 samples are superimposed on each other for comparison in Figure 16a, b. The data were obtained at low temperatures (10K) in the ordered phase using a Ge(111) analyzer. Solid lines indicate the results of scans through the $(0,2,0)$ Bragg peaks; open circles indicate scans through $(0,2.5,0)$ orbital peaks; and filled circles give the results obtained for the $(0,3,0)$ and $(0,1,0)$ reflections of the charge-ordered peaks of the $x = 0.4$ and 0.5 samples, respectively. It is clear from the figure that the Bragg and charge order peaks have similar widths, approximately corresponding to the momentum-transfer resolution at each Q . This implies that the correlation lengths of the structure and of the charge order are at least 2000 \AA in each case. The small differences in width probably reflect the Q -dependence of the resolution function. In contrast, the orbital ordering peaks in both samples are significantly broader than the resolution and imply smaller orbital domain sizes.

Estimating the correlation length, ξ , with $\xi = b/2\Delta k$, where b is the lattice constant, and Δk the half width of the orbital peaks, we find orbital correlation lengths $\xi = 320$ \AA and 160 \AA for the $x = 0.4$ and 0.5 samples, respectively. We note that in the analysis the charge order peaks were fitted with Lorentzian lineshapes, while the orbital ordering peaks were fitted with squared Lorentzians. When necessary for deconvolution, the Lorentzian squared resolution function was used, as derived from the structural Bragg peaks. These lineshapes were chosen simply for the quality of the fit, and have not been justified theoretically.

It follows that the $x = 0.4$ and 0.5 samples do not exhibit long range orbital order, but instead form a domain state with randomly distributed antiphase domain boundaries. A schematic view of such a domain wall is shown in Fig. 3c. In contrast, the charge ordering is much more highly correlated.

The presence of an orbital domain state sheds light on recent neutron diffraction studies of $\text{Pr}_{0.5}\text{Ca}_{0.5}\text{MnO}_3$ [47,25], and powdered $\text{La}_{0.5}\text{Ca}_{0.5}\text{MnO}_3$ [27]. In the former it was shown that the magnetic correlation length was finite. In $\text{La}_{0.5}\text{Ca}_{0.5}\text{MnO}_3$, which also exhibits the CE magnetic structure with orbital and charge order [4], separate magnetic correlation lengths were extracted for the Mn^{3+} and Mn^{4+} magnetic sublattices, with the remarkable result that they were quite different: $\xi_{3+}^{\text{mag}} = 250$ \AA and $\xi_{4+}^{\text{mag}} = 2000$ \AA , respectively. Those authors proposed antiphase domain walls composed of "m is-oriented" e_g orbitals to explain the magnetic disorder of the Mn^{3+} sublattice. Such domain walls break the magnetic coherence on the $3+$ sublattice only, as long as the charge order is preserved (Fig. 3c). Our results strongly suggest that this interpretation is correct, and that we have observed the antiphase domains directly in the orbital reflection (although in a different material). These results taken together suggest that such orbital domain states are common to these systems – at least in this range of doping. Note that these domains are believed to be static, and do not correspond to the (dynamic) orbital fluctuations inferred from magnetic neutron diffraction investigations of the ferromagnetic spin fluctuations in $\text{Pr}_{1-x}\text{Ca}_x\text{MnO}_3$, which disappear below T_N [47].

The temperature dependences of the orbital widths of all three samples are compared between 10 and 300 K in Fig. 17. At 10 K, the (undeconvolved) widths of the $x = 0.25, 0.4$ and 0.5 samples are about 0.0003, 0.0016 and 0.003 r.l.u., respectively, giving the correlation lengths noted above. There is a clear decrease of orbital domain size as the doping increases from $x = 0.25$ to 0.5 . A possible explanation for difference between the $x = 0.4$ and 0.5 samples follows from the fact that the $x = 0.5$ sample is closer to tetragonal than the $x = 0.4$ sample. Specifically, $(x = 0.5) = 2(a-b)/a+b = 1.48 \times 10^{-3}$ compared $(x = 0.4) = 4.23 \times 10^{-3}$ at room temperature [3]. In the more tetragonal sample, the a and b domains are more nearly degenerate and the energetic cost of a domain wall is, therefore, reduced [48]. With regard to the difference between the $x = 0.25$ sample and the $x = 0.4$ and 0.5 samples, we emphasize that the increased doping introduces charge ordering into the orbital lattice and changes the orbital periodicity (compare Figures 3a, b), and it is not clear that the two situations may be directly compared.

3. Lattice Constants and Wavevectors

The temperature dependence of the b -axis lattice constants between 10 and 300 K is shown for the $x = 0.4$ and 0.5 samples in Fig. 18. These data were obtained from measurements of the $(0,2,0)$ and $(0,4,0)$ bulk Bragg peaks. As shown in the figure, there is an abrupt change in lattice parameter of both samples at the onset of charge and orbital ordering near 250 K. This is consistent with the formation of both a cooperative Jahn-Teller distortion and a longitudinal lattice distortion as discussed in section Vb above. In the $x = 0.4$ sample, the lattice constant is approximately constant below $T_o = 245$ K, and then decreases slightly at the magnetic ordering temperature ($T_N = 170$ K). The lattice constant of the $x = 0.5$ sample increases slightly below T_o , and then levels off below T_N . These changes at T_o and T_N are greatest for the $x = 0.4$ sample, which also exhibits the longer ranged orbital order. This implies that both the orbital and magneto-striction may be partially compensated at domain boundaries, which occur more frequently in the $x = 0.5$ sample. The data obtained

for the b-axis lattice constant of the $x = 0.5$ sample are in quantitative agreement with results of Jirak et al. [25] on a powdered sample.

The temperature dependences of the charge and orbital wavevectors are plotted for the $x = 0.25, 0.4$ and 0.5 samples in Fig. 19. All wavevectors remain commensurate with the lattice and locked to either $(0,1,0)$ or $(0,1/2,0)$, throughout the ordered phase, independent of temperature to within 0.002 r.l.u. . This is in striking disagreement with the results of electron diffraction studies by Chen, et al. [24] and Jirak et al. [25], in which the orbital order wavevectors were found to change by as much as 30% . Indeed, Jirak et al. suggest the possibility of a Devil's staircase in the temperature dependence of the charge order wavevector. The results of Chen et al. [24] are schematically shown by the crosses in Fig. 19. The origin of the difference between these results and ours is not understood.

4. Scattering Above the Charge and Orbital Ordering Temperature

The behavior of the charge and orbital ordering in the vicinity of the phase transition at $T_0 = 245$ K is illustrated for the $x = 0.4$ sample in Fig. 20. Longitudinal scans were taken upon warming of the $(0,3,0)$ reflection in a π geometry and of the $(0,2.5,0)$ reflection in a $\pi/2$ geometry. The peak intensities are plotted on a logarithmic scale between 200 and 280 K in Fig. 20a. Measurable charge order fluctuations are observed at much higher temperatures above 245 K than for orbital fluctuations, with weak charge-order scattering still present at 280 K . In contrast, the orbital fluctuations fall off more quickly, and have disappeared by 260 K , at least to within the present counting statistics. The corresponding peak widths are considerably narrower for the charge order than for the orbital order (Fig. 20b), that is, the correlation lengths of the charge order fluctuations are significantly longer than those of the orbital order fluctuations at any given temperature above $T_0 = 245$ K . In this regard, it is worth noting that the correlation length of the charge order must be at least as long as that of the orbital order since the orbital unit cell is defined on the charge order lattice.

The picture these data present for the charge and orbital ordering transition in the $x = 0.4$ sample is one in which the transition proceeds via local charge order fluctuations which grow as the transition is approached from above. Long-range charge order is nucleated at the transition temperature. Orbital fluctuations are induced by the charge order fluctuations and become observable only close to the transition. The coupling mechanism has yet to be fully elucidated, however, a quadratic coupling has been suggested by Zhang and Wang [26], on the basis of a Landau theory as noted above.

The temperature dependences of the charge and orbital order half widths are plotted between 180 and 300 K for the $x = 0.5$ sample in Fig. 21a,b. The orbital scattering was characterized in a low resolution mode with a Cu (220) analyzer in the $\theta = 0$ geometry. The widths show a clear increase just below the transition, however, the signal is extremely weak and disappears about 1K above it. The charge order scattering was characterized using a higher-resolution Ge(111) analyzer. Its width also increases near the transition, however, is always smaller than the smallest value exhibited by the orbital scattering in the ordered phase. Thus, the length scale of the charge order fluctuations exceeds that of the orbital fluctuations over the narrow temperature range in which both exist. In this sense the data for the $x = 0.5$ sample are consistent with the results for the $x = 0.4$ sample, though they are neither as convincing nor as clean. Definitive conclusions will require further experiments at a more intense beam line. Preliminary results of such experiments support the suggestions made here. It is worth adding that the orbital scattering observed in the $x = 0.25$ sample was not observed to broaden, within experimental errors, at any temperature.

Finally, we note that the narrowing of the orbital reflection in the $x = 0.5$ sample below T_0 is consistent with the behavior previously seen in a number of diverse systems for which disorder prevents the particular order parameter reaching its long-range ordered ground state. Examples include magnetic order in dilute antiferromagnets in applied fields (see for example [49] and doped spin-Pierels systems [50]. In these two examples, the common phenomenology appears to be rapidly increasing time scales as the transition is approached, such that the system is not able to fully relax and reach equilibrium. As the temperature is

reduced further, equilibration times become longer than experimental measuring times and the system freezes in a metastable glass-like state. It is possible that similar phenomena underlie the behavior observed here. As noted above, the disorder is greater in the $x = 0.5$ sample. In this regard, we note that the lineshape of the orbital reflection, a Lorentzian squared, is the same as that observed in the dilute antiferromagnets. It may be derived from exponentially decaying real space correlations.

VI. MAGNETIC FIELD DEPENDENCE

An intriguing property of the perovskite manganites is the existence of colossal magnetic resistance behavior in an applied magnetic field. The transition to a metallic phase involves the delocalization of the $Mn\ e_g$ electrons, which leads to the destruction of static charge and orbital ordering. That this transition can be driven by a magnetic field in $Pr_{1-x}Ca_xMnO_3$ was first demonstrated by Tomioka, et al [31]. It is an interesting question whether the same phenomenology of the transition discussed above applies when the transition is driven at fixed temperature and the fluctuations are activated by a magnetic field. We have carried out studies of the transition at two temperatures, $T = 30$ and 200 K , with critical fields of $H_0 = 6.9(1)$ and 10.4 T , respectively [31]. The field dependence of the charge and orbital intensities of the $x = 0.4$ sample taken at $T = 30\text{ K}$ are illustrated in Fig. 22. The intensities of the $(0,3,0)$ and $(0,2.5,0)$ reflections exhibit identical field dependences below the transition. Above the transition, the charge order fluctuations are markedly stronger than the orbital fluctuations. A similar behavior was also observed at $T = 200\text{ K}$, i.e., charge order fluctuations were observed at fields for which orbital fluctuations were no longer observable (see inset, Fig. 22). From this it appears that the disorder transition is driven by charge order fluctuations for both the temperature- and field-driven cases. We note that as a result of experimental constraints it was only possible to measure the charge and orbital ordering at a photon energy of 8 keV in an applied magnetic field. The corresponding nonresonant intensities are sufficiently weak above 6.5 T that it was not possible to obtain

reliable values of the half widths.

VII. CONCLUSIONS

This paper describes a systematic study of the charge and orbital ordering in the manganite series $\text{Pr}_{1-x}\text{Ca}_x\text{MnO}_3$ with $x = 0.25, 0.4$ and 0.5 . The temperature dependence of the charge and orbital ordering was characterized in each sample, including the correlation lengths, wavevectors and lattice constants. It was found that the charge and orbital ordering are strictly commensurate with the lattice in all three samples, in striking contrast to electron diffraction studies of samples with $x = 0.5$. We do not understand the origin of these discrepancies. High Q -resolution scans revealed that long-range orbital order is never established in the $x = 0.4$ and 0.5 samples, a result that makes connections with the observation of finite Mn^{3+} magnetic domains in neutron diffraction studies of $\text{Pr}_{0.5}\text{Ca}_{0.5}\text{MnO}_3$ and $\text{La}_{0.5}\text{Ca}_{0.5}\text{MnO}_3$. We suggest that the orbital domains observed here represent the antiphase magnetic domain walls responsible for destroying the Mn^{3+} magnetic order. The observation of such an orbital glass-like state in two such materials suggests that such phenomena may be common in manganites, at least those with the CE-type charge/orbital structure. Above the charge/orbital ordering temperature T_o , we found that the charge order fluctuations are more highly correlated than the orbital ordering fluctuations. This suggests that charge order drives orbital order in these systems. In addition, we reported on the destruction of charge and orbital ordering in the $x = 0.4$ sample by the application of a magnetic field. A similar phenomenology was found for increasing field as was found for increasing temperature. Finally, the polarization and azimuthal dependence of the resonant charge and orbital ordering at the K edge is found to be qualitatively consistent with the predictions of a simple model in which the 4p levels are split in the orbitally ordered phase. The experiments do not distinguish among more sophisticated treatments of the electronic structure, whether in atomic or band limits. A new result is the discovery of a longitudinal lattice modulation in the $x = 0.4$ and 0.5 samples with scattering at both the charge and orbital

wavevectors. The presence of such a component of the modulation represents a refinement of earlier models in which the displacement was assumed to be purely transverse, following work on $\text{La}_{0.5}\text{Ca}_{0.5}\text{MnO}_3$. Similar results have been reported in $\text{Pr}_{0.5}\text{Ca}_{0.5}\text{MnO}_3$, however, there the displacement is transverse.

V III. ACKNOWLEDGEMENTS

We acknowledge helpful conversations with S. Ishihara, D. J. Khomskii, S. Maekawa, A. J. Millis, and G. A. Sawatzky. The work at Brookhaven, both in the Physics Department and at the NSLS, was supported by the U.S. Department of Energy, Division of Materials Science, under Contract No. DE-AC02-98CH10886, and at Princeton University by the NSF, under Grant No. DMR-9701991. Support from the Ministry of Education, Science and Culture, Japan, by the New Energy and Industrial Technology Development Organization (NEDO), and by the Core Research for Evolution Science and Technology (CREST) is also acknowledged. Work at the CM C beam lines is supported, in part, by the Office of Basic Energy Sciences of the U.S. Department of Energy and by the National Science Foundation, Division of Materials Research. Use of the Advanced Photon Source was supported by the Office of Basic Energy Sciences of the U.S. Department of Energy under Contract No. W-31-109-Eng-38.

REFERENCES

- [1] E. Wollan and W. Koehler, Phys. Rev. 100, 545 (1955).
- [2] J. Goodenough, Phys. Rev. 100, 555 (1955).
- [3] Z. Jirak, S. Krupica, Z. Simsa, M. Dlouha and S. Vratislav, J. Magn. Mat. 53, 153 (1985).
- [4] P. G. Radaelli, D. E. Cox, M. Marezio and S.-W. Cheong, Phys. Rev. B 55, 3015 (1997).
- [5] Y. Murakami, H. Kawada, H. Kawata, M. Tanaka, T. Arima, Y. Morimoto and Y. Tokura, Phys. Rev. Lett. 80, 1932 (1998).
- [6] Y. Murakami, J. P. Hill, D. Gibbs, M. Blume, I. Koyama, M. Tanaka, H. Kawata, T. Arima, Y. Tokura, K. Hirota and Y. Endoh, Phys. Rev. Lett. 81, 582 (1998).
- [7] S. Ishihara and S. Maekawa, Phys. Rev. Lett. 80, 3799 (1998).
- [8] M. Fabrizio, M. A. Litarelli and M. Benfatto, Phys. Rev. Lett. 80, 3799 (1998).
- [9] I. S. El'mov, V. I. Anisimov and G. A. Sawatsky, Phys. Rev. Lett. 82, 4264 (1999).
- [10] Y. Endoh, K. Hirota, S. Ishihara, S. Okamoto, Y. Murakami, A. Nishizawa, T. Fukada, H. Kimura, H. Nohiri, K. Kaneoko and S. Maekawa, Phys. Rev. Lett. 82, 4328 (1999).
- [11] P. Fuke, J. Phys. Soc. Jpn. 5, 154 (2000).
- [12] P. Wochner et al., Unpublished.
- [13] M. v. Zimmermann, J. P. Hill, D. Gibbs, M. Blume, D. Casa, B. Keimer, Y. Murakami, Y. Tomioka and Y. Tokura, Phys. Rev. Lett. 83, 4872 (1999).
- [14] L. Paololini, C. Vettier, F. de Bergevin, D. Mannix, W. Neubeck, A. Stunault, F. Yakhov, J. M. Honig and P. A. Metcalf, Phys. Rev. Lett. 82, 4719 (1999).
- [15] H. Nakao et al., Unpublished, .

- [16] B. Keimer, D. Casa, A. Ivanov, J.W. Lynn, M.v. Zimmermann, J.P. Hill, D. Gibbs, Y. Toguchi and Y. Tokura, cond-mat/0002014, .
- [17] Y. Wakabayashi, Y. Murakami, I. Koyama, T. Kimura, Y. Tokura, Y. Morimoto, K. Hirota, and Y. Endoh, Preprint, (2000).
- [18] Y. Tanaka, T. Inami, T. Wakamura, H. Yamachi, H. Omoderon, K. Ohoyama, and Y. Yamaguchi, J. Phys. Condens. Matter 11, L505 (1999).
- [19] K. Hirota, N. Oumi, T. Matsumura, H. Nakao, Y. Wakabayashi, Y. Murakami, and Y. Endoh, Phys. Rev. Lett. 84, 2706 (2000).
- [20] K. Nakamura, T. Arina, A. Nakazawa, Y. Wakabayashi, and Y. Murakami, Phys. Rev. B 60, 2425 (2000).
- [21] P. Hatton, Bulletin, Stefan University 11, 337 (1999).
- [22] M. Benfatto, Y. Joly, and C.R. Natoli, Phys. Rev. Lett. 83, 636 (1999).
- [23] S. Ishihara and S. Maekawa, Phys. Rev. B 58, 13442 (1998).
- [24] C.H. Chen, S. Mori and S.-W. Cheong, Phys. Rev. Lett. 83, 4792 (1999).
- [25] Z. Jirak, F. Damay, M. Hervieu, C. Martin, B. Raveau, G. Andre and F. Bouree, Phys. Rev. B. 61, 1181 (2000).
- [26] F. Zhang and Z.D. Wang, cond-mat/9910448, .
- [27] P.G. Radaelli, D.E. Cox, L. Capogna, S.-W. Cheong and M. Marezio, Phys. Rev. B 59, 14440 (1999).
- [28] R. Wang, J. Gui, Y. Zhu and A. Moodenbaugh, preprint .
- [29] C.H. Chen and S.-W. Cheong, Phys. Rev. Lett. 76, 4042 (1990).
- [30] Y. Okimoto, Y. Tomioka, Y. Onose, Y. Otsuka and Y. Tokura, Phys. Rev. B 57, R9377 (1998).

- [31] Y. Tomioka, A. Asamitsu, H. Kawahara, Y. Morimoto and Y. Tokura, Phys. Rev. B 53, 1689 (1996).
- [32] Y. Tokura and Y. Tomioka, J. Magn. Magn. Mater. 200, 1 (1999).
- [33] D. Gibbs, M. Blume, D. R. Harshman and D. B. McWhan, Rev. Sci. Instrum. 60, 1655 (1988).
- [34] T. Mizokawa, D. I. Khomskii and G. A. Sawatzky, Phys. Rev. B 61, R3776 (2000).
- [35] T. Hotta and E. Dagotto, cond-mat/9912469, (2000).
- [36] M. Blume, in Resonant Anomalous X-ray Scattering (North-Holland, Amsterdam, 1991), p. 495.
- [37] J. P. Hannon, G. T. Trammell, M. Blume and D. Gibbs, Phys. Rev. Lett. 61, 1245 (1988).
- [38] P. Benedetti, J. V. D. Brink, E. Pavarini, A. Vignante, and P. Wochner, Unpublished.
- [39] M. Takahashi, J. Igarashi and P. Fulde, J. Phys. Soc. Jpn. 68, 2530 (1999).
- [40] H. Yoshizawa, H. Kikano, Y. Tomioka and Y. Tokura, Phys. Rev. B 52, R13145?? (1995).
- [41] V. Kiryukhin, D. Casa, J. P. Hill, B. Keimer, A. Vignante, Y. Tomioka and Y. Tokura, Nature 386, 813 (1997).
- [42] Y. Murakami et al., Unpublished, .
- [43] S. Ishihara and S. Maekawa, Phys. Rev. B 62, xxxx (2000).
- [44] M. Takahashi, J. Igarashi and P. Fulde, cond-mat/0003066.
- [45] D. Cox, P. G. Ruedelli, M. Marezio, and S.-W. Cheong, Phys. Rev. B 57, 3305 (1998).
- [46] C. S. Nelson, M. v. Zimmermann, J. P. Hill, D. Gibbs, D. Casa, B. Keimer, T. Gog, and C. Venkataraman, Unpublished work.
- [47] R. Kajimoto, T. Kakeshita, Y. Ohara, H. Yoshizawa, Y. Tomioka and Y. Tokura, Phys.

Rev. B 58, R11837 (1998).

[48] A. Mills, Private Communication, .

[49] J.P. Hill, Q. Feng, R.-J. Birgeneau, and T.R. Thurston, Z. Phys. B 92, 285 (1993).

[50] Y.J. Wang, V. Kityukhin, R.J. Birgeneau, T. Masuda, I. Tsukada, and K. Uchinokura, Phys. Rev. Lett. 83, 1676 (1999).

FIGURES

FIG . 1. Schematic structure of $\text{Pr}_{1-x}\text{Ca}_x\text{MnO}_3$. Small spheres correspond to oxygen, and large spheres to Pr or Ca. The Mn atoms are at the center of the octahedra. Solid lines show the orthorhombic unit cell used in this paper.

FIG . 2. Composition-temperature phase diagram of $\text{Pr}_{1-x}\text{Ca}_x\text{MnO}_3$ in zero magnetic field (following reference [3]).

FIG . 3. Schematic of the charge, orbital and magnetic order in $\text{Pr}_{1-x}\text{Ca}_x\text{MnO}_3$. Filled circles represent Mn^{4+} ions, shaded figure-eights represent Mn^{3+} ions, and the arrows indicate the in-plane components of the magnetic ordering. Solid lines show orbital order unit cell; dashed lines show the charge order unit cell. (a) Proposed orbital ordering for $x=0.25$, (b,c) Charge and orbital order for $x=0.4$ and 0.5 , and (c) shows an orbital antiphase domain wall.

FIG . 4. Upper panel: Schematic view of the orbital in the a-b plane of the LaMnO_3 . Lower panel: Schematic energy level diagram of $\text{Mn } 4p_{x,y,z}$ in the orbitally ordered state, for the two orbital sublattices.

FIG . 5. Upper: Scan along $(0,k,0)$ of the $x=0.25$ sample at $T=300\text{ K}$ at the resonance Energy ($E=6.547\text{ keV}$). Lower: Scan along $(0,k,0)$ for the $x=0.4$ sample at $T=30\text{ K}$ ($E=8\text{ keV}$).

FIG . 6. Intensity plotted versus incident photon energy of the orbital (010) reflection of the $x=0.25$ sample near the Mn white line at 6.547 keV . These data were taken at APS beam line 9ID with an energy resolution of 1.5 eV . Inset: Close-up of the pre-edge feature at 6.535 keV .

FIG . 7. Polarization-resolved scans of intensity plotted versus incident photon energy of the orbital $(0,1.5,0)$ and $(0,2.5,0)$ reflections of the $x=0.4$ sample near the Mn K-absorption edge.

FIG . 8. Intensity plotted versus incident photon energy of the charge $(0,3,0)$ and orbital $(0,2.5,0)$ reflections of the $x=0.4$ sample for three different values of the azimuthal angle. The feature at $E=6.62\text{ keV}$ and $\theta=0$ in the charge order scattering is attributed to multiple scattering.

FIG . 9. Azimuthal dependence of the charge and orbital ordering intensities both on and off the Mn K-edge resonance, as obtained for the $x=0.4$ sample.

FIG . 10. Polarization-resolved scans of the intensity plotted versus incident photon energy of the charge $(0,1,0)$ and $(0,3,0)$ reflections of the $x=0.4$ sample near the Mn K-absorption edge.

FIG . 11. Intensity plotted versus incident photon energy of the charge $(0,1,0)$ reflection of the $x=0.5$ sample, near the Mn K-absorption edge.

FIG . 12. (a) Real and imaginary parts of a generic scattering factor for Mn^{3+} plotted near the K edge. $\text{Im}(f_2^d)$ is shifted by 2 eV to obtain the corresponding scattering factor for Mn^{4+} . (b) Intensity plotted versus incident photon energy including the Jahn-Teller distortion of the oxygen octahedra and using the scattering factors shown in (a). (c) Same as in (b), but now including a longitudinal Mn displacement.

FIG . 13. Temperature dependence of the scattering at the orbital $(0,3,0)$ reflection of the $x=0.25$ sample. Open circles represent data taken on X 22C, open squares taken at beam line X 21. The data sets have been scaled to agree at room temperature.

FIG . 14. Upper: Temperature dependence of the scattering at the charge $(0,3,0)$ reflection of the $x=0.4$ sample. Open circles were obtained on resonance and closed circles off resonance. Lower: Temperature dependence of the scattering at the orbital $(0,1.5,0)$ and $(0,2.5,0)$ reflections of the $x=0.4$ sample. The data at the $(0,1.5,0)$ reflection (open circles) were obtained on resonance at the Mn K-edge, while that at the $(0,2.5,0)$ reflection (closed circles) were obtained off-resonance. Note that resonant scattering at the $(0,1.5,0)$ reflection is dominated by the orbital d_{xy} contribution in Fig. 7, and not that of the lattice modulation.

FIG . 15. Upper: Temperature dependence of the scattering at the orbital $(0,1.5,0)$ reflection of the $x=0.5$ sample. Circles and squares were obtained with a Ge(111) analyzer, triangles with a Cu(220) analyzer. Lower: Temperature dependence of the scattering at the charge $(0,1,0)$ reflection obtained with a Ge(111) analyzer.

FIG .16. Upper: Longitudinal scans of the Bragg $(0,2,0)$, the charge $(0,1,0)$, and the orbital $(0,2.5,0)$ reflections of the $x=0.4$ sample at $T=8\text{ K}$. Lower: The same for the $x=0.5$ sample. Data have been normalized to the same peak intensity to facilitate comparison.

FIG .17. Temperature dependence of the halfwidths-at-half maximum of the orbital $(0,1,0)$ reflection of the $x=0.25$ (diamonds), $x=0.4$ $(0,1.5,0)$ reflection (squares) and $x=0.5$ reflection (circles) samples. Note: These widths represent the raw data, i.e., without corrections for resolution effects.

FIG .18. Temperature dependence of the b -axis lattice constants of the $x=0.4$ (open) and $x=0.5$ (closed) samples.

FIG .19. Temperature dependence of the orbital and charge wavevectors measured in all three samples. Crosses give the results of electron diffraction studies of a sample with $x=0.5$ taken from reference [24].

FIG .20. (a) Temperature dependence of the peak intensities of the $(0,3,0)$ charge order peak (closed circles) and the $(0,2.5,0)$ orbital order peak (open circles) of the $x=0.4$ sample. (b) Temperature dependence of the halfwidths-at-half maximum.

FIG .21. Temperature dependence of the undeconvolved halfwidths-at-half maximum of the scattering at the orbital $(0,2.5,0)$ and charge $(0,1,0)$ reflections of the $x=0.5$ sample.

FIG .22. Magnetic field dependence of the charge and orbital ordering intensities of the $x=0.4$ sample obtained at 30 K . Inset: Charge and orbital order superlattice reflections at $T=198\text{ K}$ and 11 T .

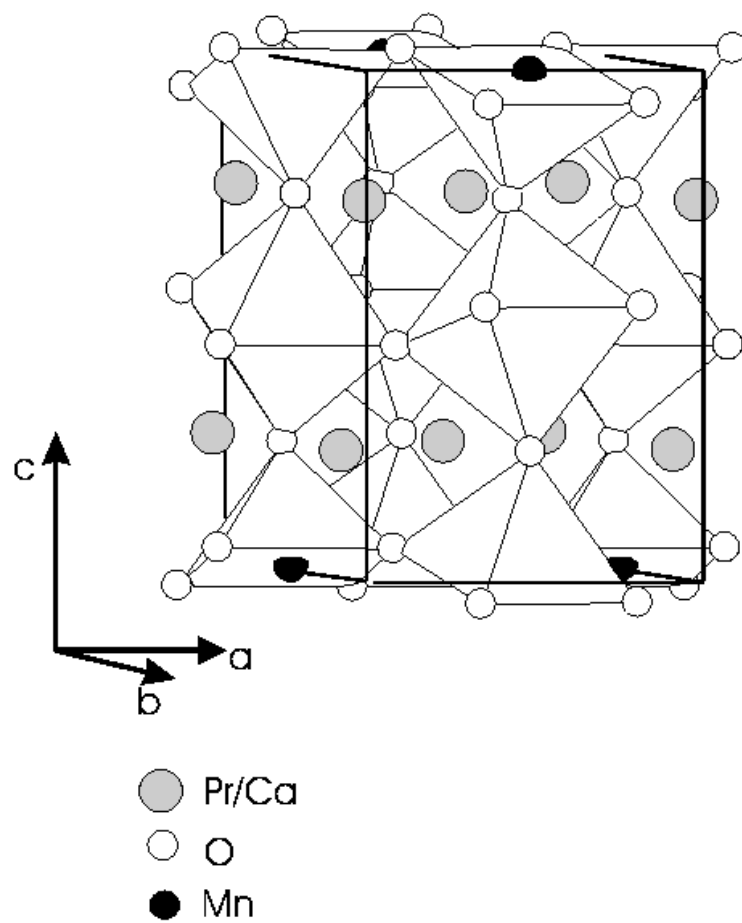


Figure 1: M. v. Zimmermann *et al.*

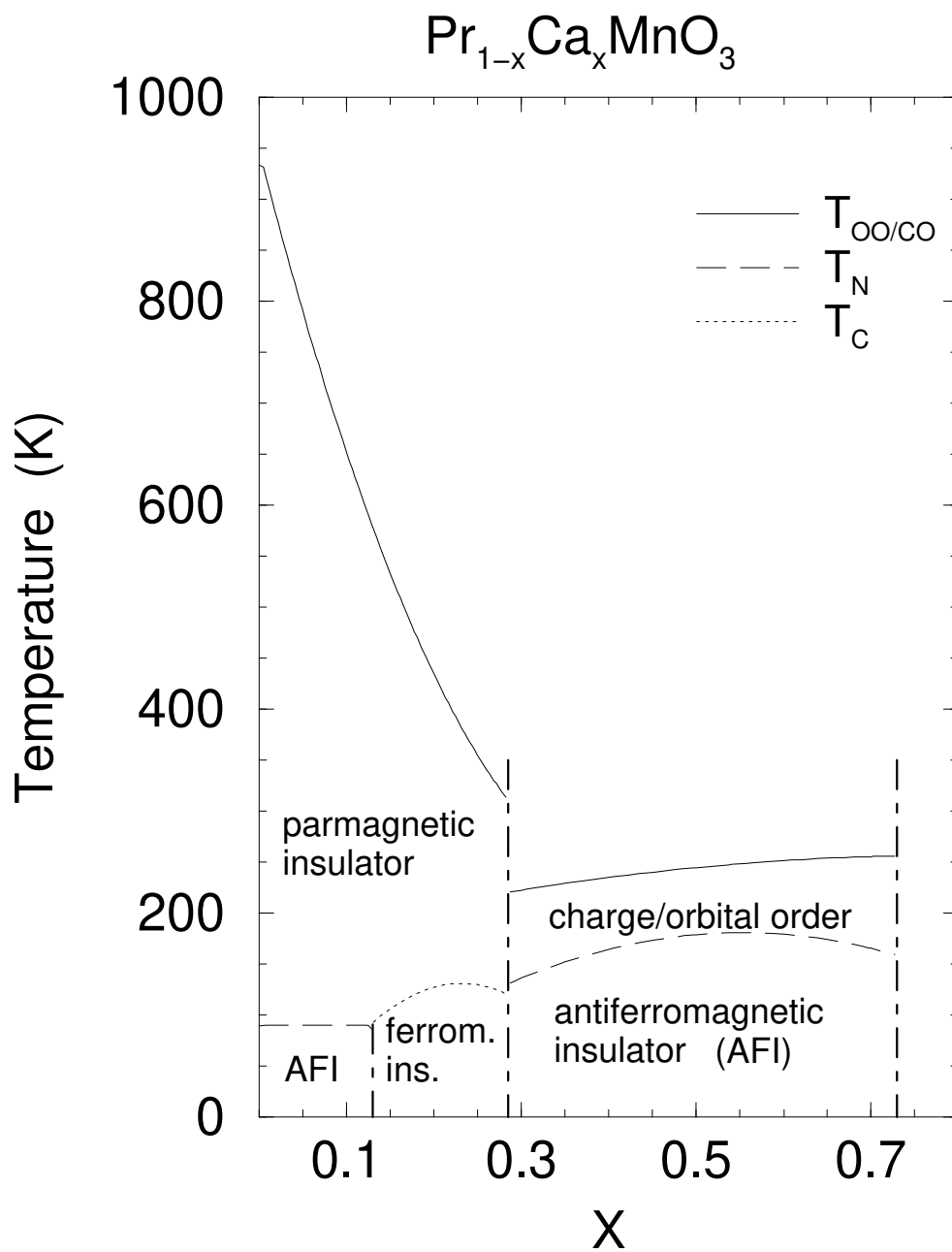


Figure 2: M. v. Zimmermann *et al.*

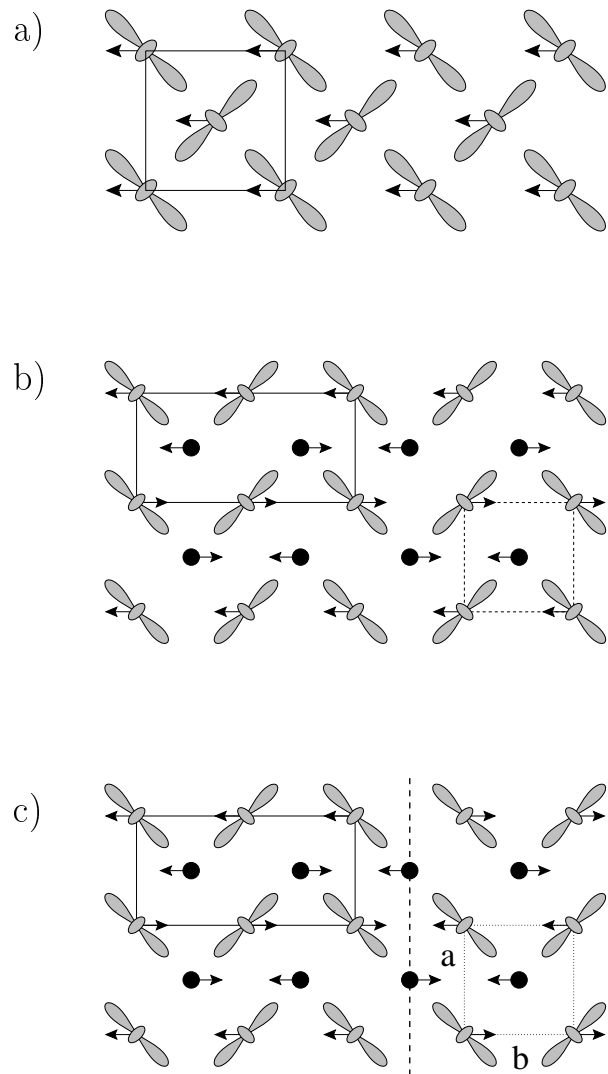


Figure 3: M. v. Zimmermann *et al.*

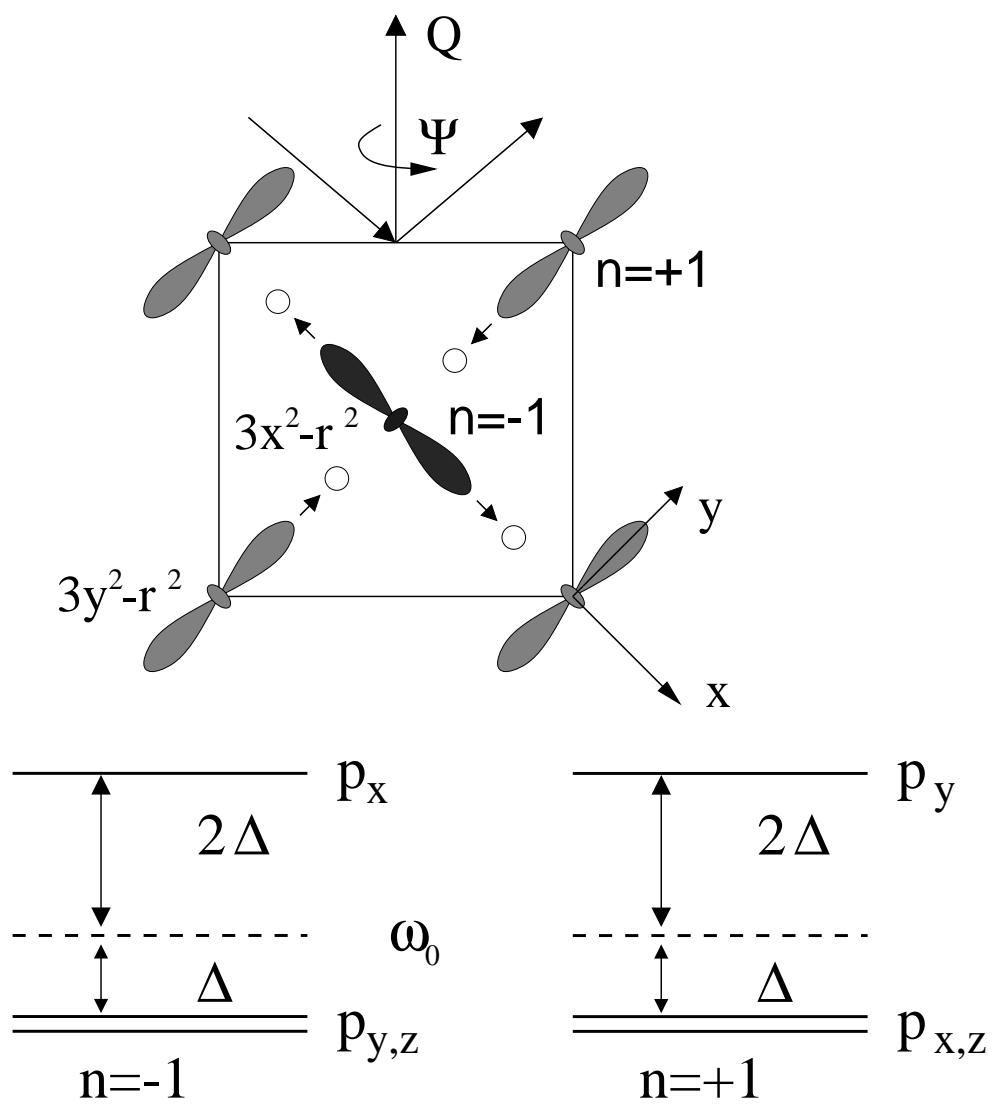


Figure 4: M. v. Zimmermann *et al.*

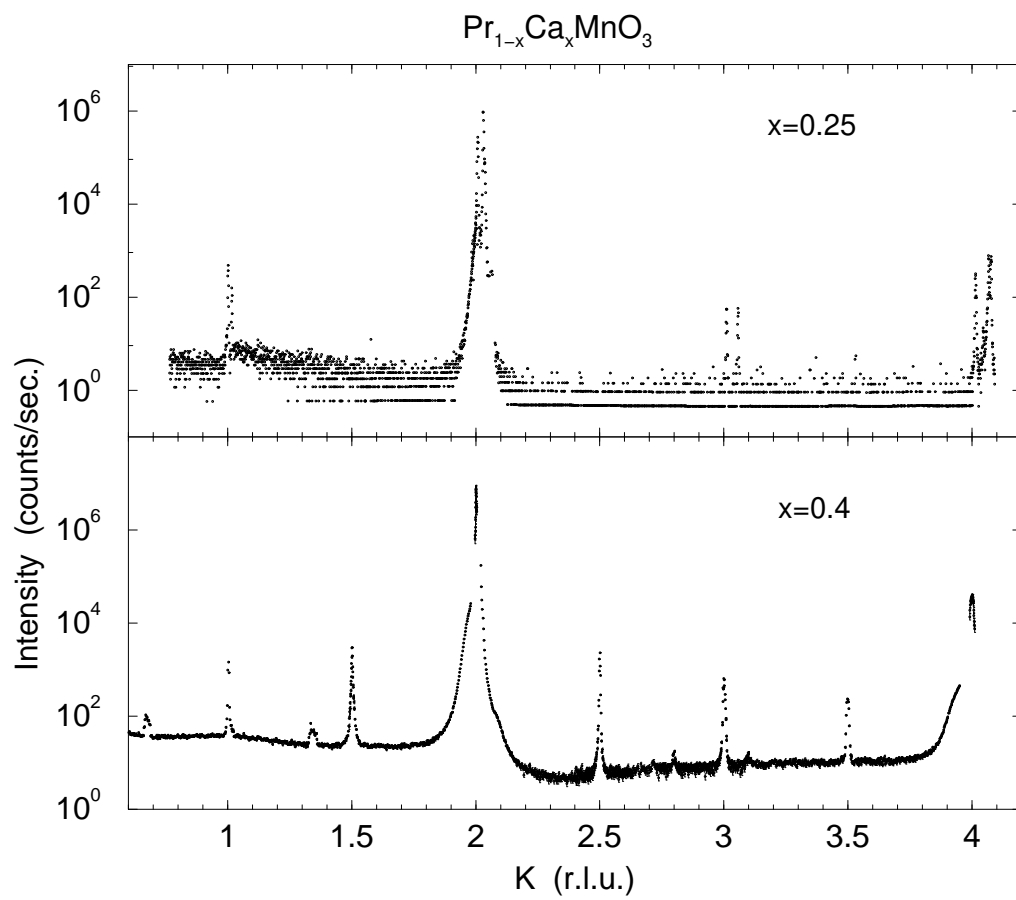


Figure 5: M. v. Zimmermann *et al.*

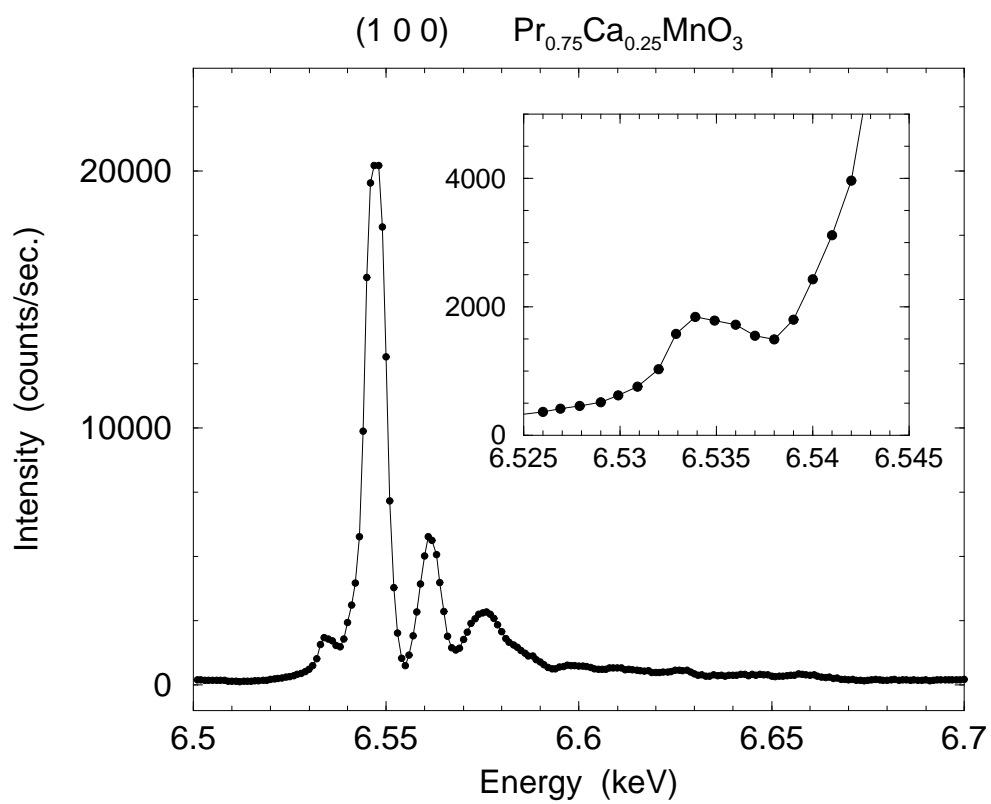


Figure 6: M. v. Zimmermann *et al.*

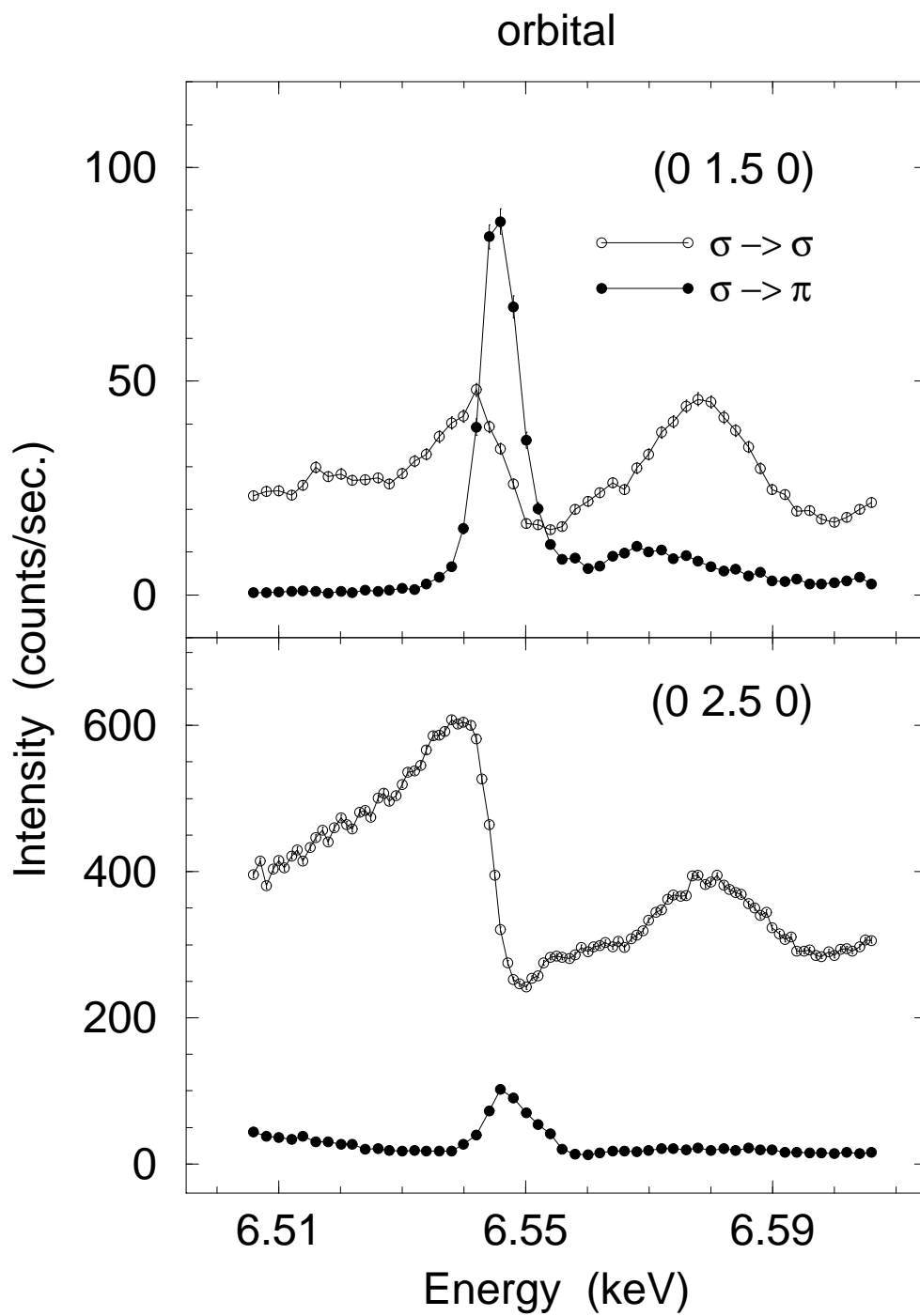


Figure 7: M. v. Zimmermann *et al.*

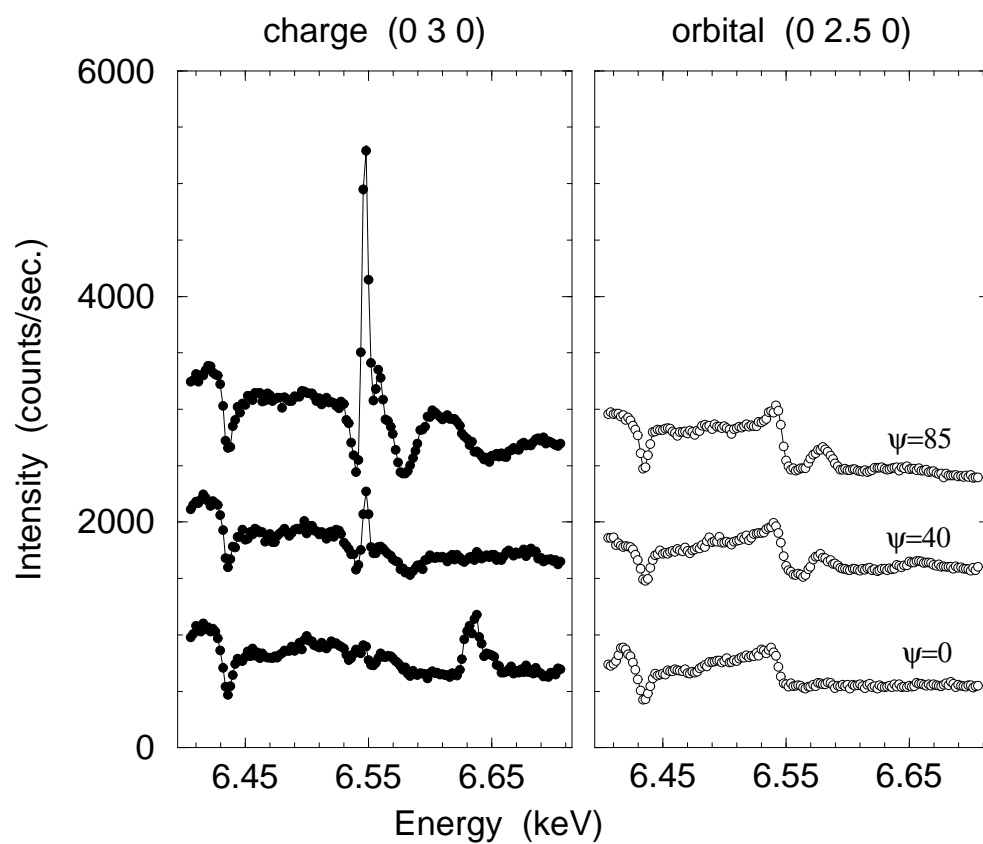


Figure 8: M. v. Zimmermann *et al.*

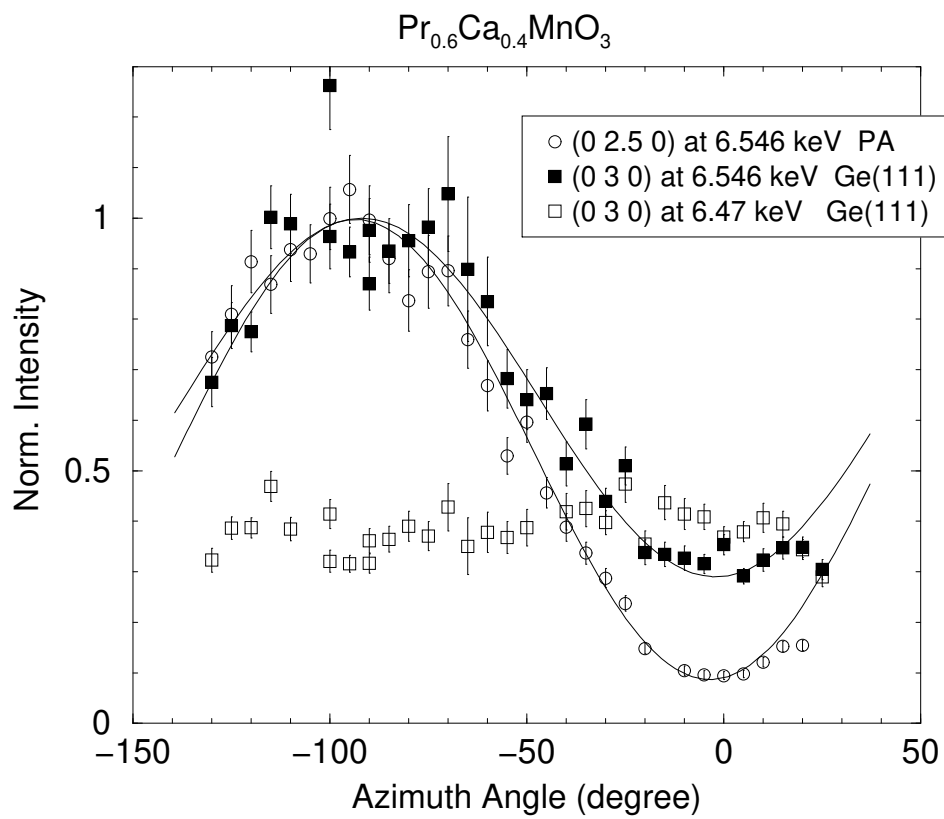


Figure 9: M. v. Zimmermann *et al.*

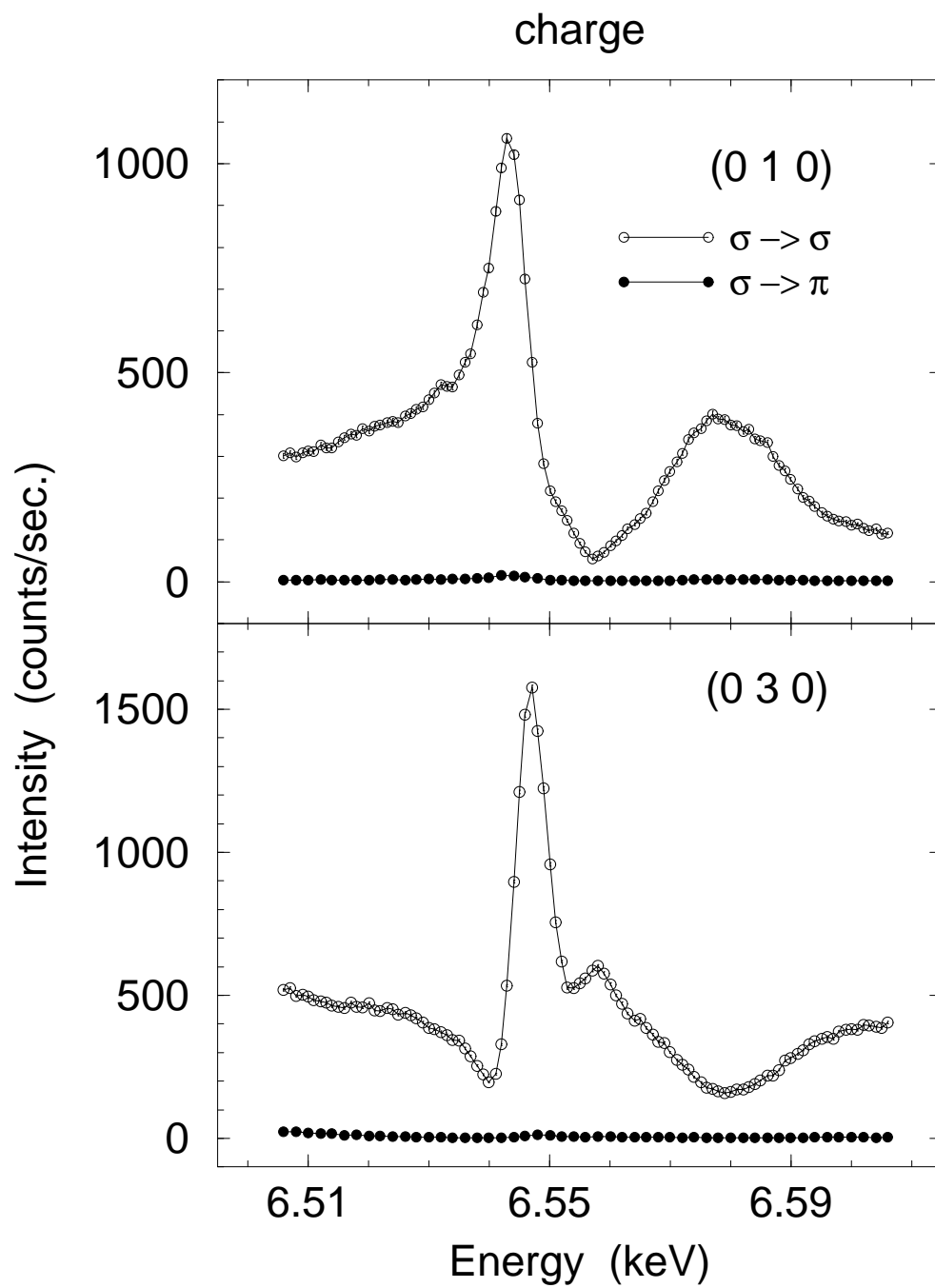


Figure 10: M. v. Zimmermann *et al.*

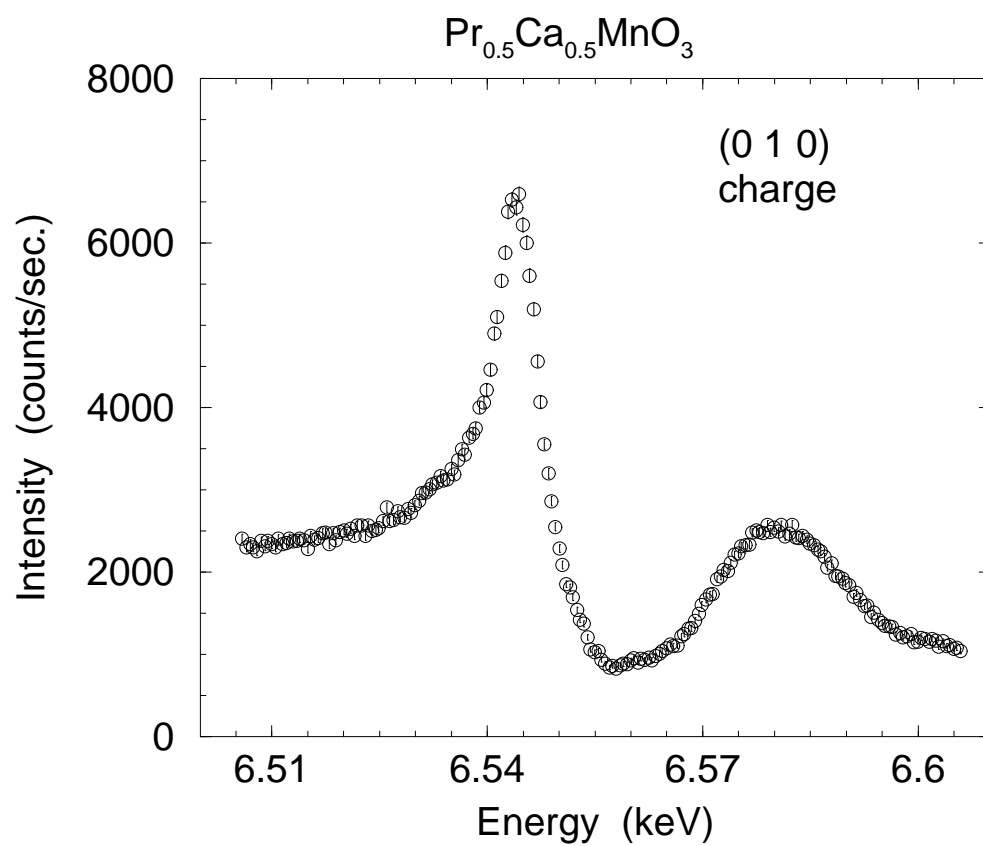


Figure 11: M. v. Zimmermann *et al.*

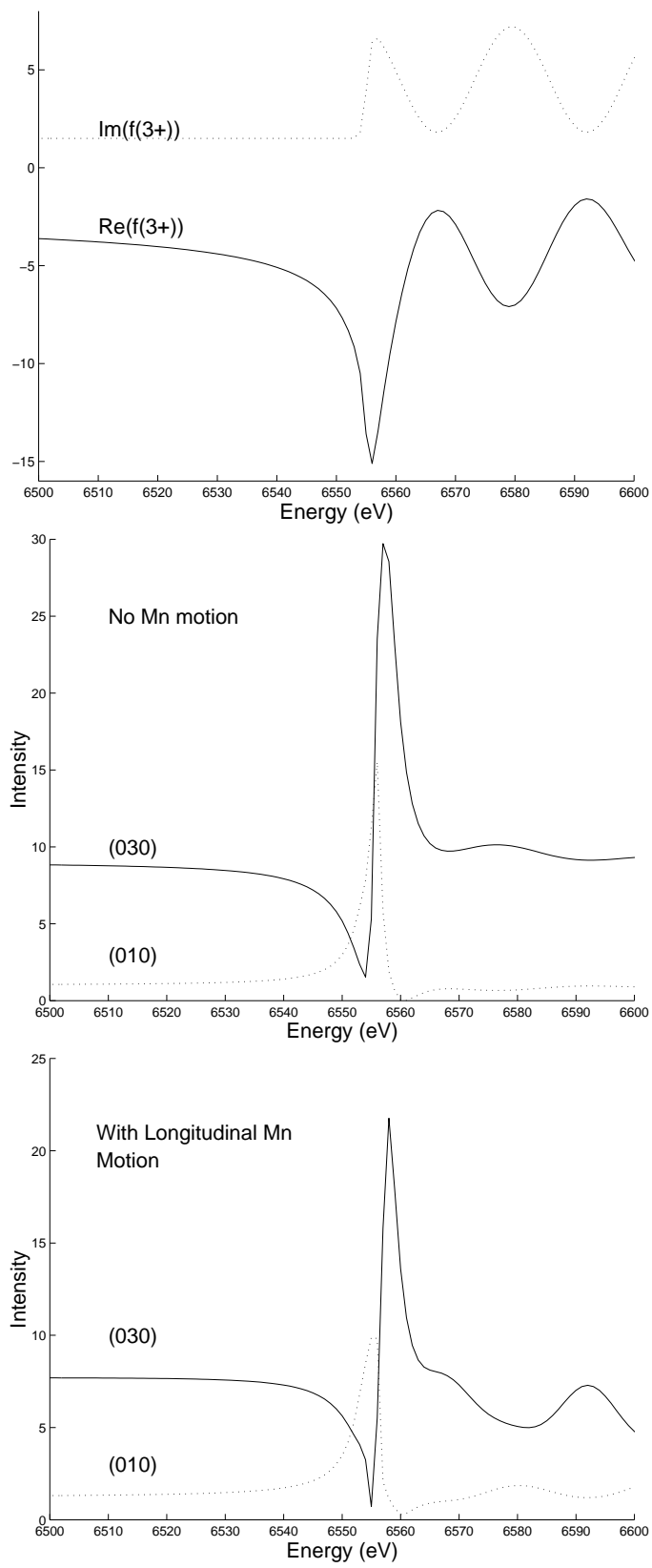


Figure 12: M. v. Zimmermann *et al.*

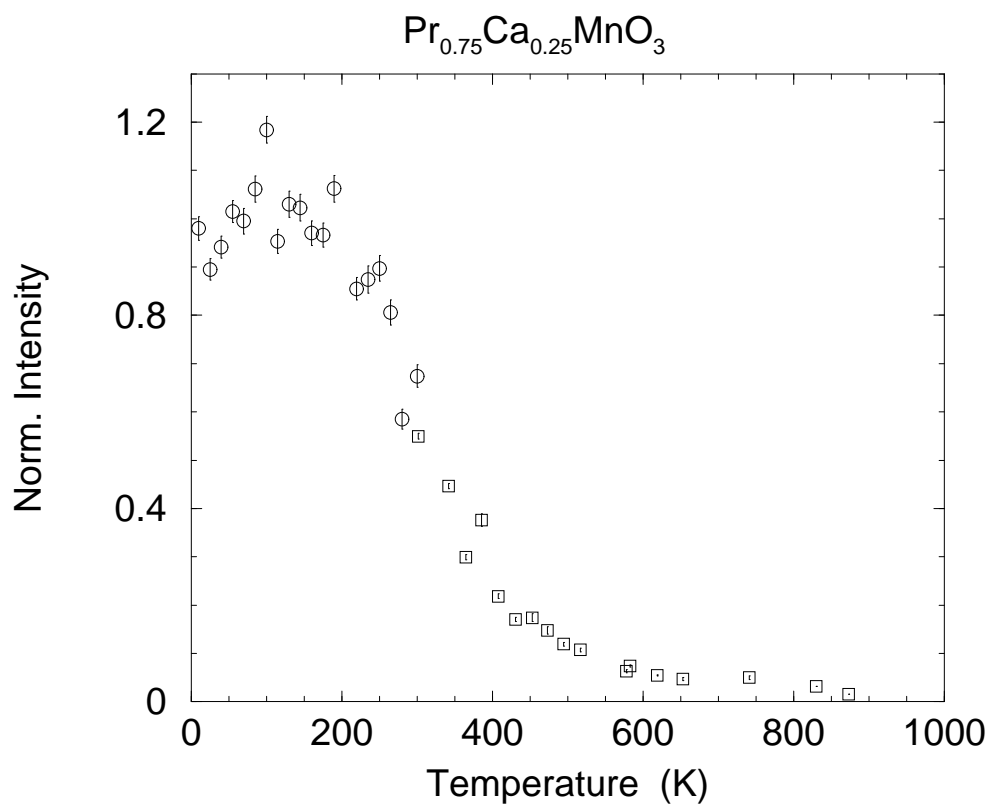


Figure 13: M. v. Zimmermann *et al.*

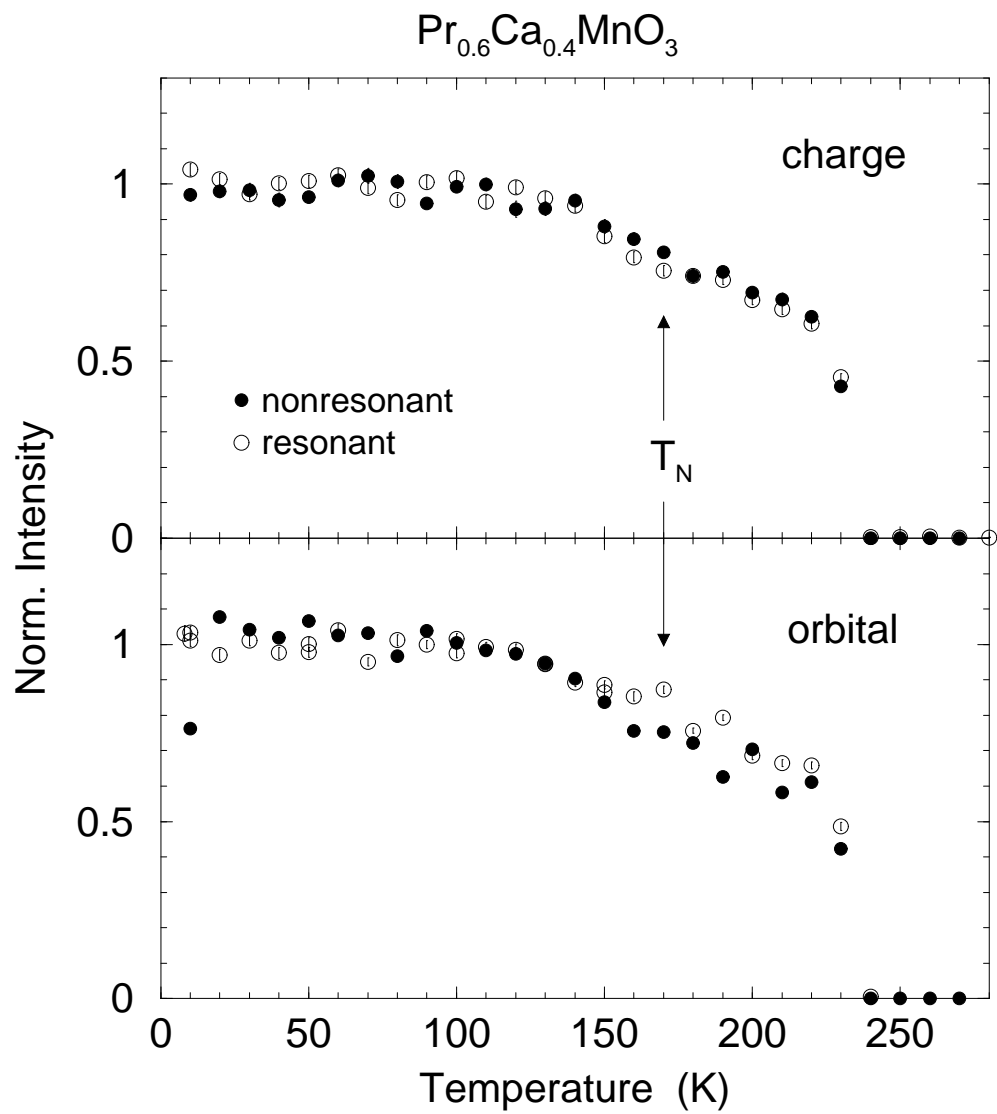


Figure 14: M. v. Zimmermann *et al.*

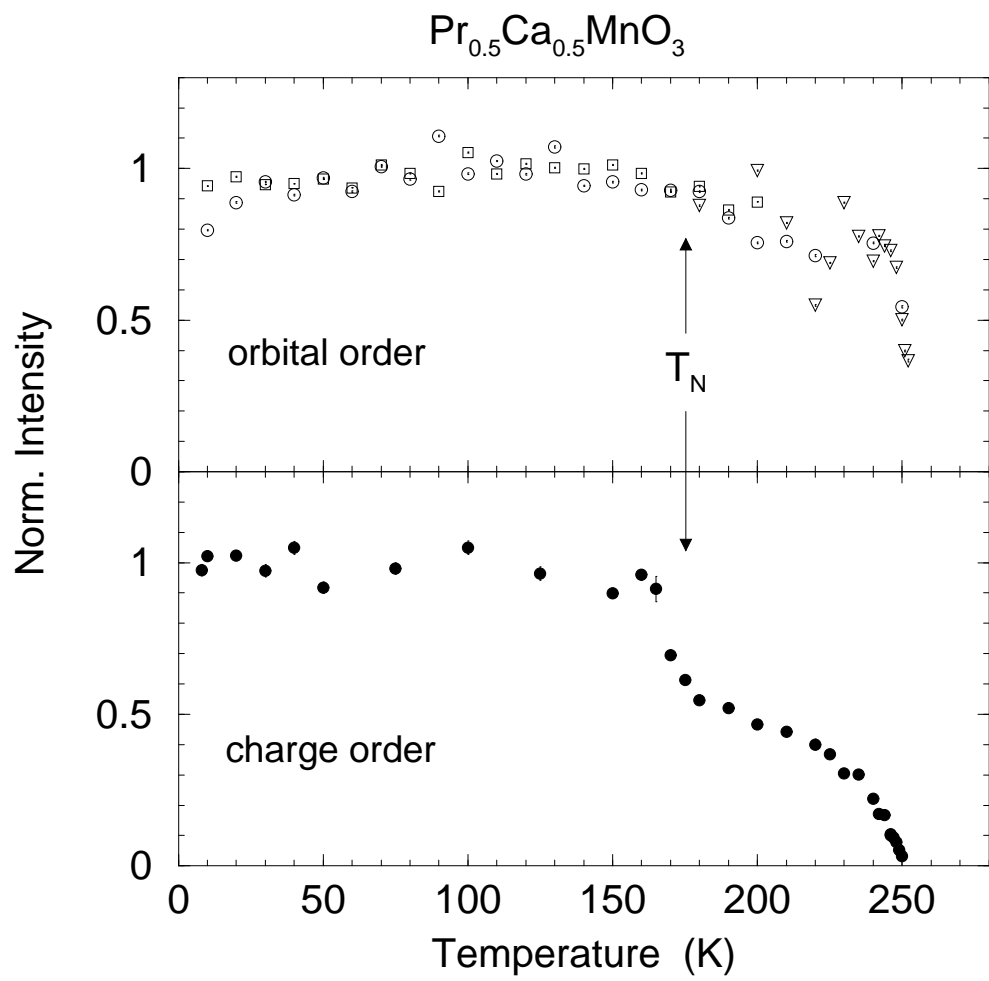


Figure 15: M. v. Zimmermann *et al.*

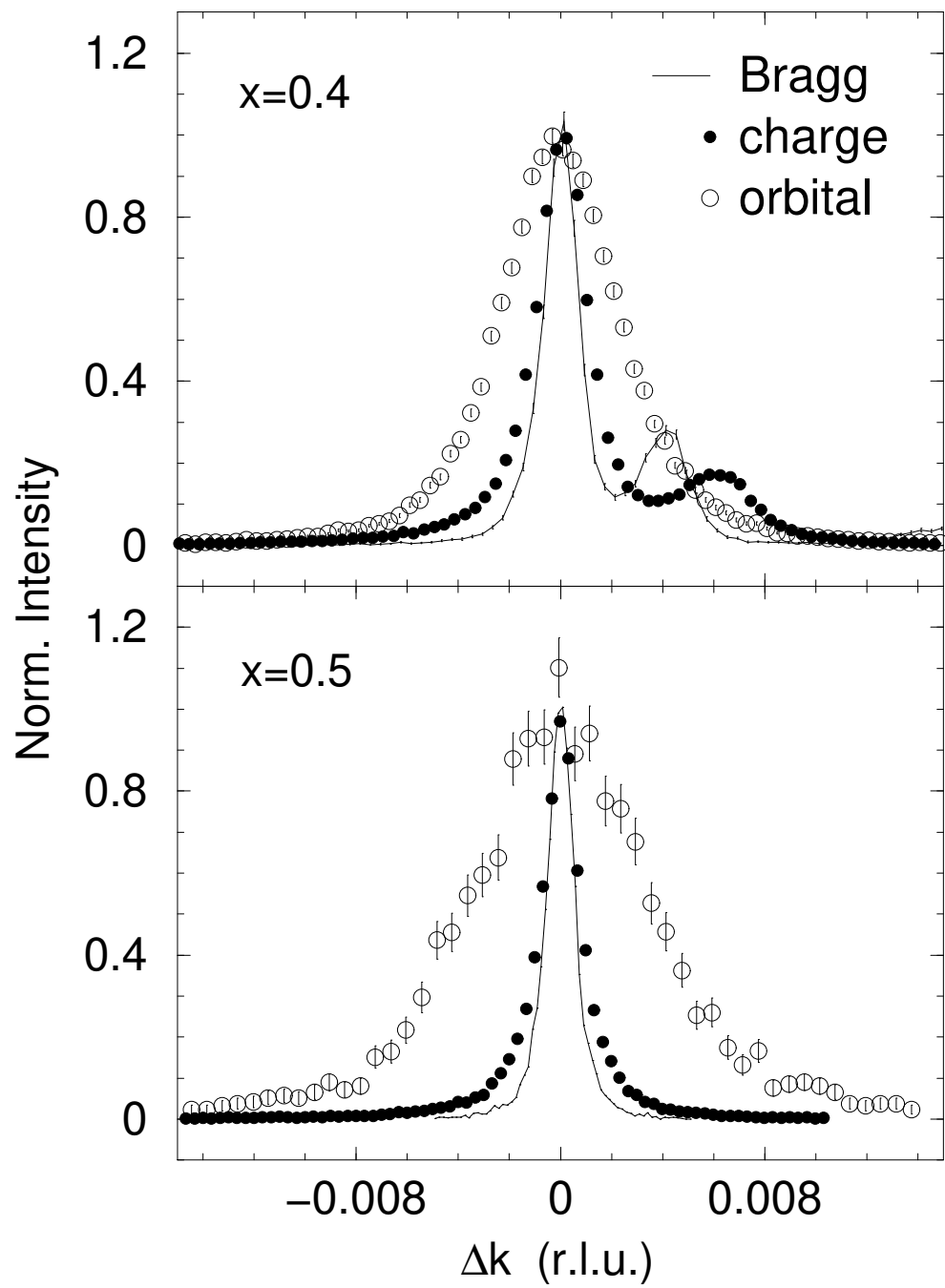


Figure 16: M. v. Zimmermann *et al.*

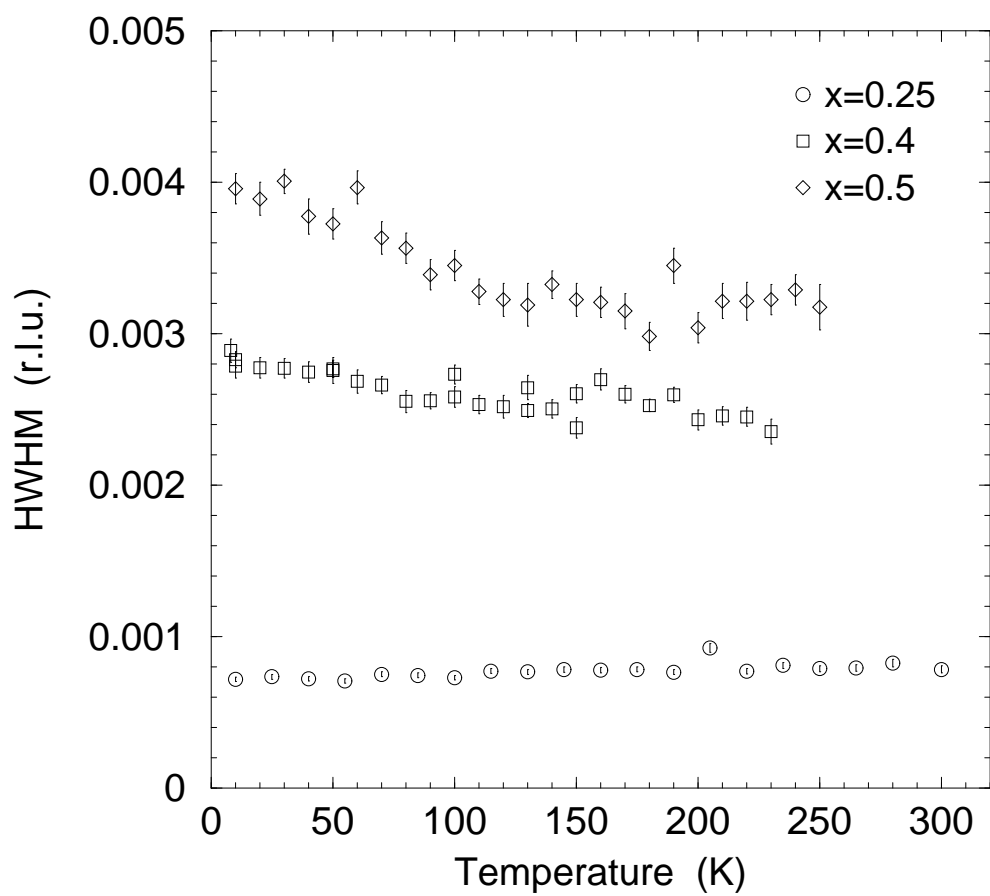


Figure 17: M. v. Zimmermann *et al.*

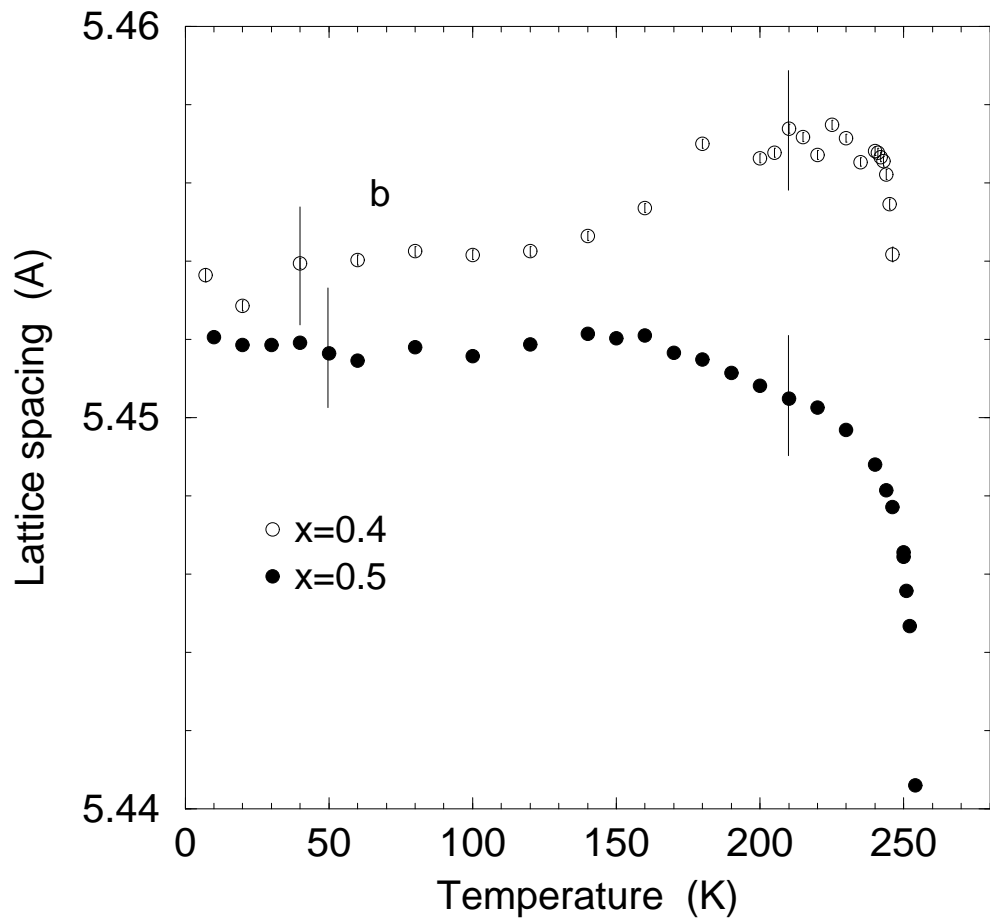


Figure 18: M. v. Zimmermann *et al.*

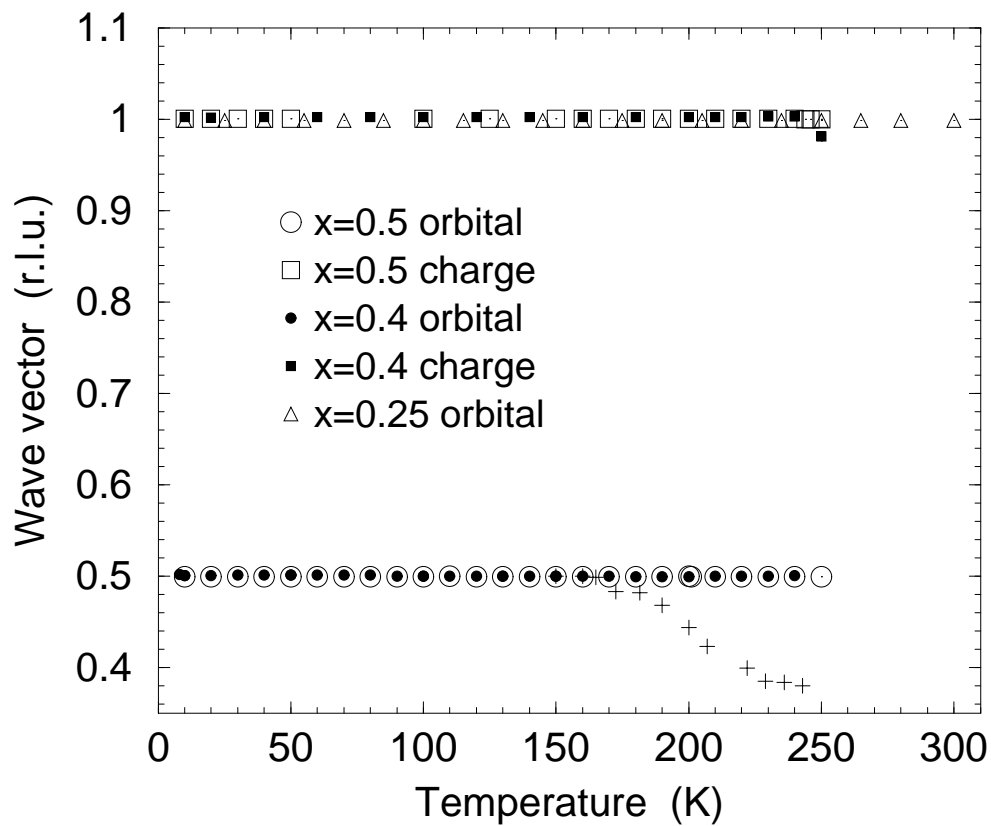


Figure 19: M. v. Zimmermann *et al.*

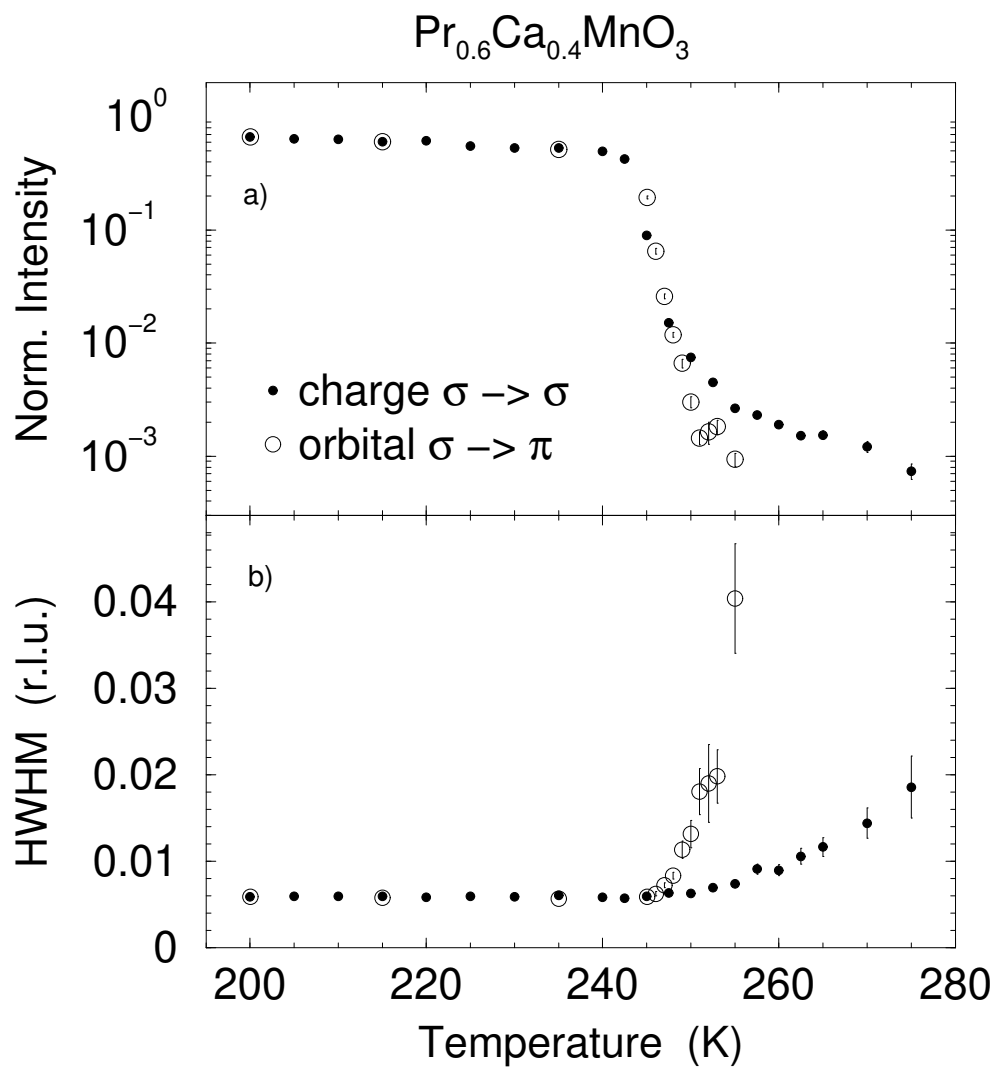


Figure 20: M. v. Zimmermann *et al.*

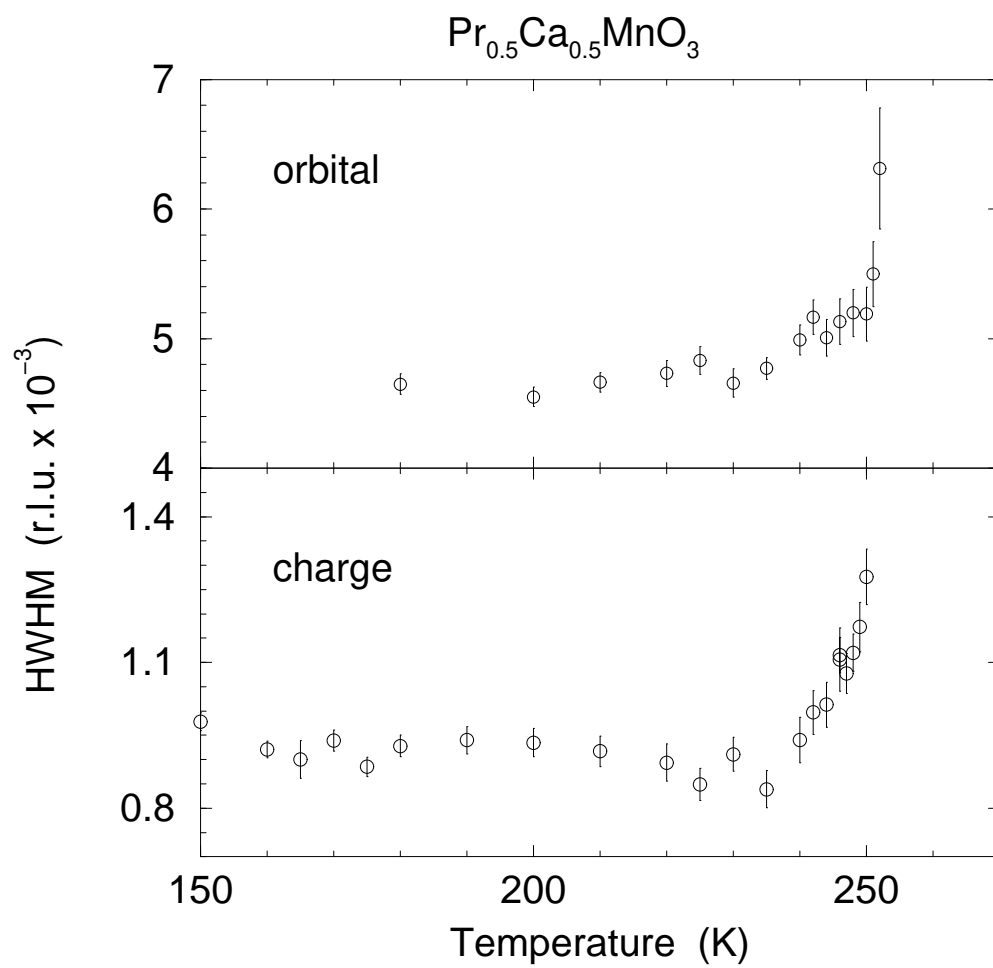


Figure 21: M. v. Zimmermann *et al.*

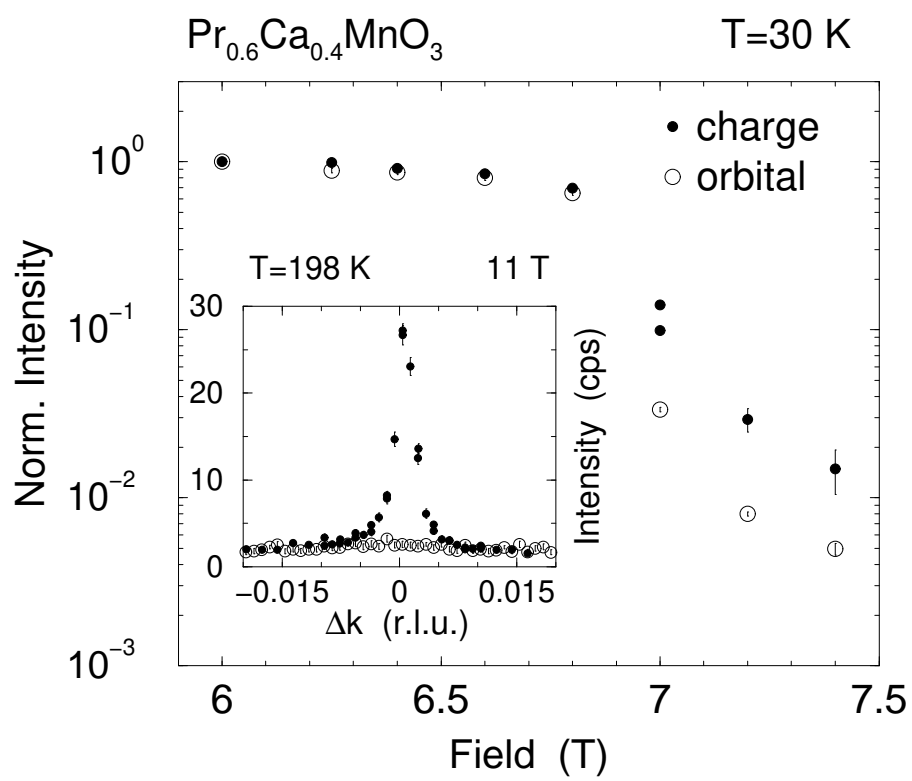


Figure 22: M. v. Zimmermann *et al.*